This is a preprint, the final version is subject to change, of the American Mineralogist (MSA)
Cite as Authors (Year) Title. American Mineralogist, in press.
DOI: https://doi.org/10.2138/am-2019-6604

Revision 1. *In situ* high-temperature vibrational spectra for synthetic and natural clinohumite: implications for dense hydrous magnesium silicates in subduction zones

Dan Liu[1], Youwei Pang[1], Yu Ye[1]*, Zhenmin Jin[1], Joseph R. Smyth[2], Yan Yang[3], Zengming Zhang[4], Zhongping Wang[4]

[1]State Key Laboratory of Geological Processes and Mineral Resources, China University of Geosciences, Wuhan, 430074, China

[2]Department of Geological Sciences, University of Colorado, Boulder, Colorado, 80309, USA

[3]Department of Earth Sciences, Institute of Geology and Geophysics, Zhejiang University, Hangzhou, 310058, China

[4]Physics Experiment Teaching Centers, University of Science and Technology of China, Hefei, 230026, China

*Contacting email: yeyu@cug.edu.cn

Abstract: Clinohumite is a potentially abundant silicate mineral with high water concentration (2~3 wt.% H_2O), which is generated from dehydration of serpentine-group minerals in subduction zones. Previous studies show that fluorine substitution ($OH^- = F^-$) can stabilize clinohumite to significantly higher temperature in subduction zones, although temperatures within the slabs are thought to be well within the stability field of both F-bearing and OH-clinohumite. We collected *in situ* high-temperature Raman and Fourier transform infrared (FTIR) spectra for both the synthetic [$Mg_9Si_4O_{16}(OH)_2$] and natural [$Mg_{7.84}Fe_{0.58}Mn_{0.01}Ti_{0.25}(SiO_4)_4O_{0.5}(OH)_{1.30}F_{0.20}$] clinohumite samples up to 1243 K. Three OH bands above 3450 cm^{-1} are detected for both the natural and synthetic samples with negative temperature dependence, due to neighboring H-H repulsion in the crystal structure. Additional OH peaks are detected for the natural sample below 3450 cm^{-1} with positive temperature dependence, which could be explained by non-polar F^- substitution in the OH site. Hence, F^- substitution significantly changes the high-temperature behavior of hydrogen bonds in the humite-group minerals. On the other hand, we evaluated the mode Grüneisen

parameters (γ_{iP}, γ_{iT}), as well as the intrinsic anharmonic parameters (a_i) for clinohumite, chondrodite, and phase A, the dense hydrous magnesium silicate (DHMS) phases along the brucite-forsterite join. The estimated averaged anharmonic parameters (a_{i_avg}) for these DHMS phases are systematically smaller than those of olivine. In order to model the thermodynamic properties of minerals (such as heat capacity) at the high temperature conditions of the mantle, the DeBye model, which simply approximates the lattice vibrations as harmonic oscillators, is commonly used. In contrast to forsterite, such quasi-harmonic approximations are valid for clinohumite at subduction zone temperatures, as the anharmonic contribution is no more than 2% when extrapolated to 2000 K. Hence, the classic DeBye model can reasonably simulate the thermodynamic properties of these DHMS phases in subduction zones.

Key words: clinohumite; F substitution; Grüneisen parameter; anharmonicity; subduction slab; DHMS phases

1. Introduction

Plate subduction is a geodynamic process that can transport water in the form of hydrous minerals from the surface reservoir down into the upper mantle and transition zone (Zheng 2012) and perhaps the lower mantle. Among various hydrous minerals, the serpentine-group (containing about 13wt% H_2O) would break down at pressure-temperature conditions of the upper mantle, to generate a series of dense hydrous magnesium silicate (DHMS) phases: such as Phase A ($Mg_7Si_2O_8(OH)_6$, 12 wt% H_2O), chondrodite ($Mg_5Si_2O_8(OH)_2$, 5 wt% H_2O), and clinohumite ($Mg_9Si_4O_{16}(OH)_2$, 3 wt% H_2O) on the brucite - forsterite join at pressures below 15 GPa (e.g. Wunder 1998; Berry and James 2001; Stalder and Ulmer 2001; Smyth et al. 2006). These mineral phases may further transform to phase E ($Mg_2SiO_2(OH)_4$, 10 wt% H_2O), super-hydrous phase B ($Mg_{10}Si_3O_{14}(OH)_4$, 3 wt% H_2O) and phase D ($MgSi_2O_4(OH)_2$, 10 wt% H_2O) above 15 GPa (e.g. Frost and Fei 1998; Irifune et al. 1998; Ohtani et al. 2001). These DHMS phases have been proposed as potential carriers of water into the Earth's interior (McGetchin et al. 1970; Kanzaki 1991; Faust and Knittle 1994; Wunder et al. 1995; Guo and Yoshino 2013). From the previous high-*P,T* experiments on DHMS (Yamamoto and Akimoto 1977; Wunder 1998), we derive the formation of clinohumite from dehydration of serpentine as in the chemical reactions below:

$$5\ Mg_3Si_2O_9H_4\ (serpentine) = 4\ Mg_2Si_2O_6\ (orthoproxene) + Mg_7Si_2O_{14}H_6\ (Phase\ A) + 7\ H_2O \quad (1)$$

$$Mg_7Si_2O_{14}H_6\ (Phase\ A) + 10\ Mg_2SiO_4\ (olivine) = 3\ Mg_9Si_4O_{18}H_2\ (clinohumite) \quad (2)$$

Clinohumite is an expected phase in the breakdown of serpentine at high pressure in subducting slabs (Yamamoto and Akimoto, 1977). Its stability is extended to lower pressures by the presence of Ti and F (Sánchez-Viscaino et al 2005; Shen et al 2015) so that it may become abundant under certain *P-T* condition in the mantle. In order to evaluate the potential role of these DHMS phases in subduction slabs, significant efforts have been devoted to explore the physical and chemical properties of humite-group minerals. Crystal chemistry has been studied by both single-crystal X-ray diffraction (i.e., Ribbe and Gibbs 1988; Camara 1997; Ottolini et al. 2000; Ye et al. 2015), and neutron diffraction (i.e., Berry and James 2001; Friedrich et al. 2001, 2002) for both synthetic and natural samples, to explore compositional effect on the crystal structures. The experiments on equations of state (i.e. Ross and Crichton 2001; Crichton and Ross 2002, 2005; Holl et al. 2006; Kuribayashi et al. 2008; Ye et al. 2013 and 2015; Qin et al. 2017) and elasticity (Sinogeikin and Bass 1999; Ross et al. 2001; Friedrich et al. 2002; Kuribayashi 2004) systematically show that OH concentration in these DHMS phases significantly increases the thermal expansivity and compressibility, while decreasing the elastic moduli, as well as seismic velocities. On the other hand, the interatomic vibration modes have been measured by Raman and FTIR spectra (i.e. Lin et al. 1999; Frost et al. 2007a and 2007b). So far, most of these spectral studies are conducted at high-pressure and room temperature, while limited high-temperature Raman measurements have been reported for these phases (Liu et al. 1997; Mernagh et al. 1999; Lin et al. 2000).

In this study, we focus on *in situ* high-temperature Raman and FTIR spectral measurements on both synthetic and natural clinohumite samples. The synthetic sample is pure $Mg_9Si_4O_{16}(OH)_2$ (Ye et al. 2013), whereas the natural samples generally have sigificant concentrations of F, Ti, Mn, and Fe (e.g. McGetchin et al. 1970; Fujino and Takeuchi 1978; Shen et al. 2015). We explored the effect of fluorine on the behavior of hydrogen bonds by FTIR, and the implication for the stability of clinohumite in subduction zones (Shen et al. 2015; Grützner et al. 2017). *In situ* high-temperature vibrational spectra provide experimental constraints on the mode Grüneisen parameters and intrinsic anharmonicity of clinohumite. Comparisons are also made with previous high-temperature and high-pressure experiments on chondrodite (Lin et al. 1999;

Mernagh et al. 1999), phase A (Liu et al. 1997), as well as hydrous forsterite (Hushur et al. 2009; Yang et al. 2015a). We further evaluated the effect of hydration on the anharmonic contributions to the thermodynamics properties for clinohumite, the DHMS phase generated from dehydration of serpentine-group minerals in the subduction zones.

2. Experimental procedures

2.1. Sample characterization

The colorless synthetic clinohumite (run SZ0411B from Ye et al. 2013) is assumed to have the stoichiometric composition of $Mg_9Si_4O_{18}H_2$, whereas the natural mineral, dark yellow in color, was separated from clinohumite–diopside–garnet rocks from a marble-para-gneiss unit of the Central Dabie medium-T/UHP eclogite-facies zone from the Ganjialing area (Liu 2015).

Several natural crystals with grain size of 100~200 μm were selected from the bulk rock, and polished on both sides to a thickness of 40 μm. Then, the composition was analyzed with a JEOL JXA-8100 Electron Probe Micro Analyzer equipped with four wavelength-dispersive spectrometers (WDS). An electron beam with spot size of 10 μm was focused on the surface of the sample with an accelerating voltage of 15 kV and a current of 20 nA. Data were corrected on-line using a modified ZAF (atomic number, absorption, fluorescence) correction procedure (Zhang and Yang 2016). Peak counting times were 10 s for Mg, Si, Fe, F and Cl; and 20 s for Ti and Mn, adopting the following certified standards: pyrope garnet (Fe), diopside (Mg), rhodonite (Mn), olivine (Si) , rutile (Ti), topaz (F), and sodium chloride (Cl). Totally, eleven points were measured for the weight percentages of these oxides, and the averaged values with standard deviations are listed in **Table 1**. The water content is 1.82 wt% for the natural clinohumite and 2.90 wt% for the synthetic sample. The formula of the natural sample is interpreted as: $Mg_{7.842}Fe_{0.582}Mn_{0.011}Ti_{0.250}(SiO_4)_4O_{0.500}(OH)_{1.296}F_{0.201}Cl_{0.001}$, with the Fe ratio of Fe/(Fe+Mg) = 0.069, while the synthetic sample is assumed to have the nominal composition of $Mg_9Si_4O_{18}H_2$.

Clinohumite crystallizes in space group of $P2_1/b$, which is chosen as a nonstandard setting of $P2_1/c$, in order to preserve the ***a*** and ***b*** axes of olivine. As shown in **Fig.1**, the crystal structure of clinohumite

includes five different octahedral M cation sites, noted as M1C, M1N, M25, M26 and M3, with the ratios of 1:2:2:2:2 and 2 distinct tetrahedral Si cation sites (Si1 and Si2) (e.g. Fujino and Takéuchi 1978; Ottolini et al. 2000; Berry and James 2001; Ye et al. 2013 etc). There are nine oxygen anion sites with the OFOH site hosting a monovalent anion bonded to 3 M sites (2 M3 sites and 1 M25 site). It is also noted that there are 2 distinct H sites (H1 and H2) in the structure (Abbott et al. 1989; Yamamoto and Akimoto 1997). Since H1 site is so close to the inversion center that it could not be fully occupied, H2 becomes a secondary site for a proton coordinating OFOH (Fujino and Takeuchi 1978; Berry and James 2001; Friedrich et al. 2001). The M3 site is the preferred octahedral site for Ti^{4+} by the substitution $Mg^{2+}+2OH^{-}=Ti^{4+}+2O^{2-}$, in order to relieve the need for the H2 position (Robinson et al. 1973; Ribbe 1979; Friedrich et al. 2001). Hence, in this natural clinohumite sample, 25% of the M3 sites is occupied by Ti^{4+}, while the occupancies of OH^{-}, F^{-} and O^{2-} in the OFOH sites are 65%, 10% and 25%, respectively. The M3 and OFOH sites have equal multiplicities in the unit cell of clinohumite.

2.2. *In situ* high-temperature Raman and FTIR spectroscopy

In situ high-temperature Raman spectra were measured using a Dilor XY micro-Raman system, with the LABRAM-HR spectrometer (Yang et al. 2015a). The natural and synthetic crystals, about 100×150×50 μm in size, were loaded on the sapphire plate in a Linkam TS1500 heating stage. A resistance heater was used to produce high temperature, and an S-type thermocouple was used to measure temperature with uncertainties of less than 1 K. The samples were heated from 300 K up to 1050 K, with an increment of 50 K and a heating rate of 25 K/min, which had been programmed into an automatic temperature control unit. At each step, the target temperature was held for at least 5 min for thermal equilibration before measurement. The sample chamber of the heating stage was filled with N_2 as a 'protecting gas' to avoid any potential degradation of the samples at high temperatures. The spectra at high temperatures were collected in the frequency range of 100–1200 cm^{-1} with a duration of 10 minutes. A green beam (λ = 514.5 nm) from an Ar-ion laser was used for excitation, and focused to a diameter of 10 μm onto the surface of the sample through an objective lens (50×). The spectrometer was calibrated using a single-crystal of silicon as a reference.

Unpolarized FTIR spectra were obtained from 3000 to 4000 cm^{-1} on a Nicolet iS50 FTIR spectrometer coupled with a Continuum microscope using a KBr beam-splitter and a liquid-nitrogen cooled MCT-A detector. Totally, 128 scans were accumulated for each spectrum at a resolution of 4 cm^{-1}. The aperture size was set to about 70 × 70 μm^2, which was smaller than the grain size. Measurements were made in optically clean, inclusion- and crack-free areas. Background was also collected at each step after the measurement on the sample, and the spectra collected at different temperatures on the same selected area were used for consistent comparison. Peakfit v4.12 software was adopted for the analyses of both Raman (Yang et al. 2015a) and infrared spectra (Yang et al. 2015b).

Single crystals of the clinohumite samples were mounted on the sapphire plate of an Instec HS1300 heating stage, equipped with a resistance heater and an S type thermocouple. The sample temperature was determined with a typical precision of less than 1K. The high-temperature infrared spectra were measured with a heating rate of 10 K/min and an increment of 50 K. For every temperature step, the dwell time was 5 min. Another spectrum was taken for the natural sample when the temperature was quenched to room temperature after heating.

3. Results and discussion

3.1. Raman modes at room and high temperatures

Raman spectra for both the natural and synthetic samples at ambient conditions (**Fig. 2**), and their fitted Raman bands are also given (**Table 2**). There are, in total, 191 potential vibrational modes (including 94 Raman-active modes and 97 IR-active modes) for OH-clinohumite based on space group $P2_1/c$, according to the symmetry analysis from Lin et al. (2000). These vibrational modes are divided into five groups: (1) 75 modes below 365 cm^{-1} correspond to translations of the MgO_6 octahedra and SiO_4 tetrahedra; (2) 64 modes from 380 to 700 cm^{-1} are assigned to the SiO_4 rotations and internal bending modes; (3) 16 modes from 710 to 780 cm^{-1} are ascribed to translations and rotations of OH groups; (4) 32 modes from 820 to 970cm^{-1} are attributed to the SiO_4 internal stretching modes; (5) 4 modes from 3500 to 3600 cm^{-1} are ascribed to the OH internal stretching modes. There are two fairly strong peaks at 651 and 691cm^{-1} (in the

frequency range for SiO_4 internal bending modes) were detected exclusively in the natural sample. Similarly, Ye et al (2013) also observed strong Raman peaks at 650 and 690 cm^{-1} for the Fe-bearing OH-clinohumite sample (SZ0407B), as opposed to the Mg-pure one (SZ0411B). Such difference might be explained by the effect of chemical impurity (e.g., Fe), and the incorporation of larger Fe^{2+} cations into some octahedral sites could distort neighboring SiO_4 tetrahedra to some extent. Besides, some Raman peaks are observed to be relatively more intense in the natural sample, such as the bands at 755 and 780 cm^{-1}, as well as the modes at 133, 233 and 384 cm^{-1} in the low-frequency range, which might be caused by Fe and Ti ordering into the octahedral sites.

The SiO_4 internal stretching modes at 861, 842 and 830 cm^{-1} are more intense than the other modes for the clinohumite samples (**Fig. 2**), and such strong SiO_4 modes are also observed for olivine (Gillet et al. 1991; Yang et al. 2015a), chondrodite (Lin et al. 1999; Mernagh et al. 1999), humite (Frost et al. 2007a), norbergite (Liu et al. 1999), and Phase A (Liu et al. 1997), etc. Based on the selection rules of Raman spectroscopy, the incident light induces an instantaneous dipole moment through deforming the electron cloud around the molecule, and the intensity of the Raman mode depends on how easily the electron cloud can be deformed, i.e. the polarizability of the electron cloud (Colthup et al. 1964). Hence, the strong SiO_4 internal stretching modes suggest the high polarizability of the oxygen environments in the SiO_4 tetrahedron (Yang et al. 2015a).

High-temperature Raman spectra were obtained from room temperature up to 1050 K for both the natural and synthetic samples, and the selected Raman spectra are shown in **Fig. 3 (a, b)**, respectively. Despite some bands becoming quite broad at high temperature, most of the peaks remain distinguishable throughout the temperature range, allowing fair fitting of peak positions. For the natural sample, the intensities of the bands at 133, 233 and 384 cm^{-1} increase at high temperature range of 400 ~ 850K. The synthetic sample persisted up to 1050 K in this study, whereas Lin et al. (2000) reported that synthetic clinohumite can persist up to 873K. The Raman spectra of the samples quenched from 1050 K are also compared in **Fig. 3 (a,b)** for both the samples. Most of the peaks measured before and after heating do not shift significantly. However, the intensities of some peaks become significantly weaker for the natural sample: the peaks at 133, 233, 384 cm^{-1} associated with lattice vibration, as well as the ones at 755, 780

187 cm^{-1} attributed to $M^{2+}OH$ deformation. This might be explained by the order-disorder transition for Fe or Ti
188 at certain high temperature, and the disorder arrangement was maintained during the fast quenching process
189 after heating to 1050 K.

190 Variation of the Raman shift frequencies with temperature for both the natural and synthetic samples
191 are plotted in **Fig. 4 (a-c)**. The bands systematically shift to lower frequencies with increasing temperature
192 except for the weak band at 744 cm^{-1} in the synthetic sample. Fairly linear regressions are recognized
193 between the Raman shifts and temperature for both these samples throughout the measured temperature
194 range up to 1050 K. The temperature dependences of these Raman modes, $(\partial v_i/\partial T)_P$, are listed in **Table 2**.

195

196 **3.2. FTIR at ambient temperature**

197 The FTIR spectra of the clinohumite samples obtained at ambient conditions are compared in **Fig. 5**,
198 and the fitted peak positions for the OH-stretching bands are listed in **Table 2**. The OH-stretching bands
199 frequency (cm^{-1}) are controlled by the hydrogen bond length ($d_{O...H}$, Å), and Libowitzky (1999) proposed an
200 empirical formula as below:

201 $$d_{O...H} = -0.2146 \times Ln\left(\frac{3632 - v_i}{1.79 \times 10^6}\right) \quad (3)$$

202 Three OH bands around 3609, 3560, 3526 cm^{-1} are observed for both the natural and synthetic
203 clinohumite samples, which were also reported in previous FTIR (Liu et al. 2003; Frost et al. 2007b) and
204 Raman (Lin et al. 2000; Frost et al. 2007a; Ye et al. 2013; Shen et al. 2014) measurements, as compared in
205 **Table 3**. These OH bands corresponds to $d_{O...H}$ of 2.09 ~ 2.41 Å, which is consistent with the structure
206 refinement on the deuterated hydroxyl-clinohumite sample by neutron powder diffraction (Berry and James
207 2001) (**Table 4**). No extant Raman or FTIR studies of clinohumite report OH-stretching frequencies above
208 3615 cm^{-1} corresponding to hydrogen bond lengths greater than 2.5 Å (**Table 3**.)

209 Alternatively, additional bands in natural clinohumite are detected at 3161, 3233, 3309, 3397 and 3436
210 cm^{-1} (1.77 ~ 1.96 Å for $d_{O...H}$), while no OH bands are observed below 3450 cm^{-1} for the synthetic sample.
211 In addition, Shen et al. (2014) also reported an OH band at 3393 cm^{-1} for natural F-bearing clinohumite.

Similar phenomena were also observed in chondrodite: for synthetic OH-chondrodite, OH bands were only detected above 3450 cm^{-1} ($d_{O...H}$ > 2 Å) (e.g. Akaogi and Akimoto 1980; Liu et al. 2003; Kuribayashi et al. 2004); while for natural F-bearing samples, more peaks around 3380 ~ 3390 cm^{-1} (1.90 ~ 1.91 Å for $d_{O...H}$) were observed as well as the ones above 3450 cm^{-1} (e.g. Williams 1992; Cynn et al. 1996; Kuribayashi et al. 2004; Prasad and Sarma 2004).

It is proposed that the hydrogen bonds are elongated due to the H-H repulsion between the adjacent OH pair in the crystal structures of the humite-group minerals (Lin et al. 1999 and 2000; Liu et al. 1999; Hushur et al. 2009), as shown in the **Fig. 6**. While in the natural samples, some of the OH^- groups are replaced by F^- anions. Such H-H repulsion would vanish if the neighboring OH^- group is substituted by F^- anion, and then the hydrogen bond length becomes shortened, with the OH bands shifting to lower frequencies (below 3450 cm^{-1}).

3.3. FTIR spectra at high temperatures

High-temperature FTIR spectra were collected at temperatures up to 1093 K for the synthetic clinohumite sample. Breakdown occurred while the sample was subsequently heated to 1143 K. On the other hand, the natural sample survived up to 1243 K, due to F incorporation (Engi and Lindsley 1980; Khodyrev et al. 1992; Grützner et al. 2017) (**Fig. 7**). The main OH bands survived after high temperature heating and the integral absorbance for the OH bands in the frequency range of 3000 - 3700 cm^{-1} remained almost the same as that before heating, suggesting no significant dehydration at high temperatures up to 1243 K (Paterson 1982; Libowitzky and Rossman 1997; Balan et al. 2008). Overall, the OH bands generally become broader and weaker at higher temperature (e.g. Suzuki and Nakashima 1999; Zhang et al. 2007; Yang et al. 2010, 2015b). While in this measurement, the main OH bands around 3309, 3397, 3526, 3560 and 3610 cm^{-1} remained distinguishable at high temperatures, except that the weak peak around 3610 cm^{-1} overlapped severely with the one at 3560 cm^{-1} above 900 K, and could not be fitted separately. The variations of the frequencies with temperature are plotted in **Fig. 8** with nearly linear regressions, and the fitted temperature derivatives ($cm^{-1} \cdot K^{-1}$) for these OH bands are listed in **Table 2**.

For both the synthetic and natural clinohumite samples, the OH bands above 3450 cm^{-1} systematically shifted to lower frequencies with increasing temperature, with the slopes of -0.23~-0.28 ($cm^{-1}\cdot K^{-1}$) for the strong peaks around 3530 and 3560 cm^{-1}, and -0.44 ($cm^{-1}\cdot K^{-1}$) for the weak peak at 3610 cm^{-1}. Negative temperature dependence for the OH bands above 3450 cm^{-1} also has been reported for the humite-group minerals (i.e., Lin et al. 2000 for OH-clinohumite; Mernagh et al. 1999 for chondrodite; and Liu et al. 1999 for norbergite). Such phenomena at high temperature are consistent with the positive pressure dependence for the OH bands above 3450 cm^{-1} (i.e. Lin et al. 1999 and 2000; Liu et al. 1999 and 2003; etc.). This special behavior for the humite-group minerals at high temperatures and high pressures could be explained by the H-H repulsion between the adjacent OH pairs (Lin et al. 1999 and 2000). During thermal expansion at high temperatures, the H-H repulsion becomes weaker at larger atomic distance, and hydrogen atoms move backward against elongation of the hydrogen bond (**Fig. 6**). Hence, $d_{O\cdots H}$ bond lengths decrease with increasing temperature. Similarly, $d_{O\cdots H}$ increase at higher pressure, due to the enhancement of the H-H repulsion at shorter atomic distance upon compression.

Conversely, the peaks at 3310 and 3400 cm^{-1} for the natural sample show positive temperature dependence, instead, because the H-H repulsion vanishes due to the replacement of the neighboring OH^- by F^-. Then, the $d_{O\cdots H}$ bond lengths increase at higher temperature (shifting to higher frequencies), which is common for the hydrogen bonds in most of hydrous silicate minerals. The hydrogen bonds in hydrous phases generally become shortened at higher pressure, and the OH stretching bands shift to lower frequency, such as in H_2O ice polymorphs (e.g. Abebe and Walrafen 1979; Walrafen et al. 1982), brucite (e.g. Duffy et al. 1995), Phase A (e.g. Liu et al. 1997), Phase D (e.g. Shieh et al. 2009 for OH bands above 3000 cm^{-1}), Phase E (e.g. Kleppe et al. 2001; Shieh et al. 2009), hydrous forsterite (e.g. Hushur et al. 2009), hydrous wadsleyite (e.g. Liu et al. 1998; Kleppe et al. 2006), hydrous ringwoodite (e.g. Kleppe et al. 2002; Yang et al. 2014), and so on.

It should be noted that Williams (1992) and Kuribayashi et al. (2004) also reported positive pressure dependence for the OH bands above 3450 cm^{-1}, while negative pressure dependence for the OH bands below 3450 cm^{-1} in natural F-bearing chondrodite at high pressure. Such high-pressure behavior of natural chondrodite is consistent with our high-temperature observations on the natural clinohumite sample.

3.4. Grüneisen Parameters and Intrinsic Anharmonicity

There are two parts of the contribution to the temperature- and pressure- dependence of the frequency (v_i): pure volume variation at high temperature / pressure and pure temperature / pressure contribution arising from intrinsic anharmonicity (Gillet et al. 1991; Okada et al. 2008; Yang et al. 2015a). The Grüneisen parameters in isobaric (γ_{iP}) and isothermal (γ_{iT}) modes, as well as the intrinsic anharmonicity (a_i), are derived in Eqns (4-6):

$$\gamma_{iP} = \left(\frac{\partial \ln v_i}{\partial \rho}\right)_P = -\frac{1}{\alpha \cdot v_{0i}}\left(\frac{\partial v_i}{\partial T}\right)_P \quad (4)$$

$$\gamma_{iT} = \left(\frac{\partial \ln v_i}{\partial \rho}\right)_T = \frac{K_T}{v_{0i}}\left(\frac{\partial v_i}{\partial P}\right)_T \quad (5)$$

$$a_i = \left(\frac{\partial \ln v_i}{\partial T}\right)_V = -\alpha \cdot (\gamma_{iP} - \gamma_{iT}) \quad (6)$$

Where v_{0i} are the mode frequencies at ambient conditions, while ($\partial v_i/\partial T$) and ($\partial v_i/\partial P$) are the temperature and pressure derivatives of the frequency (v_i), respectively. α is the thermal expansion coefficient, and K_T is the isothermal bulk modulus at ambient condition. The intrinsic anharmonic parameter (a_i) is significant in thermodynamic systems, which show the anharmonicity induced by temperature and pressure.

Adopting the averaged volume thermal expansion coefficients of 36.8×10^{-5} K^{-1} for synthetic clinohumite and 34.9×10^{-5} K^{-1} for the natural sample from Ye et al. (2013), we calculate the mean isobaric Grüneisen parameters (γ_{iP}) for the Raman (100 ~ 1000 cm^{-1}) and IR (3000 ~ 4000 cm^{-1}) modes. On the other hand, Lin et al. (2000) measured high-pressure Raman spectra for Mg-pure OH-clinohumite.

By combing extant results of high-pressure Raman scattering of Mg end member OH-clinohumite (Lin

et al. 2000) and the isothermal bulk modulus K_T = 119.47 GPa determined by Crichton and Ross(2002), we can also derive the isothermal Grüneisen parameters (γ_{iT}), as well as the corresponding intrinsic anharmonicity (a_i). The mode Grüneisen and intrinsic anharmonicity parameters for clinohumite are listed in **Table 2**.

The isobaric Grüneisen parameters (γ_{iP}) for both the natural and synthetic clinohumite samples from this study are compared with those for phase A (Liu et al. 1997), OH-chondrodite (Mernagh et al. 1999), as well as hydrous forsterite (C_{H2O} = 0.9 wt.%; Yang et al. 2015a) in **Fig. 9(a)**. To simplify the calculation, linear regressions between frequencies and temperature are fitted for the Raman modes measured at high temperatures, and the mean thermal expansion coefficients are adopted for phase A (Pawley et al. 1995), chondrodite (Ye et al. 2015), and hydrous forsterite (Ye et al. 2009). Pressure dependence for the Raman modes also has been measured for OH-clinohumite (Lin et al. 2000), OH-chondrodite (Lin et al. 1999), phase A (Liu et al. 1997) and hydrous forsterite (Hushur et al. 2009). We calculated the isothermal Grüneisen parameters (γ_{iT}), as in Eqn (5), from the reported isothermal bulk moduli for synthetic OH-clinohumite and OH-chondrodite (Ross and Crichton 2001), phase A (Crichton and Ross 2002), as well as hydrous forsterite (Smyth et al. 2005). The γ_{iP} modes parameters for these hydrous phases are also compared in **Fig. 9(b)**.

For phase A, chondrodite, clinohumite and hydrous forsterite, the isobaric (γ_{iP}) and isothermal (γ_{iT}) Grüneisen parameters range 0.4 ~ 3 for the lattice vibration modes, -0.4 ~ 2.2 for the SiO_4 bending modes, 0 ~ 1 for the SiO_4 stretching modes, and -0.3 ~ 0.3 for the OH stretching modes, respectively. The mode Grüneisen parameters (γ_{iP} and γ_{iT}) for the lattice vibrations are generally greater than those for the SiO_4 stretching modes, since the bond strength of Mg-O is weaker than that for Si-O, and MgO_6 octahedra show larger thermal expansivity and compressibility than SiO_4 tetrahedra in silicate minerals (e.g. Smyth et al. 2004; Qin et al. 2017). Besides, the mode Grüneisen parameters for OH stretching are close to zero, and even smaller than those for the SiO_4 stretching vibrations.

Based on the derived isobaric and isothermal mode Grüneisen parameters, we can further calculate the intrinsic anharmonicity parameters (a_i) for OH-clinohumite, phase A, OH-chondrodite, as well as forsterite, which are compared in **Fig. 10**. In the frequency range of the SiO_4 stretching modes (800-1000 cm^{-1}),

312 which are the most intense in the Raman spectra, chondrodite and phase A systematically show higher a_i
313 parameters (but smaller in absolute values) than clinohumite and hydrous forsterite. That is because the
314 measured γ_{iP} Grüneisen parameters for chondrodite and phase A (Liu et al. 1997; Mernagh et al. 1999) are
315 lower than those for clinohumite and hydrous forsterite (this study; Yang et al. 2015a) (**Fig. 9a**). Besides,
316 phase A and clinohumite also show higher a_i parameters (but smaller in absolute values) than hydrous
317 forsterite in the range of lattice vibrations below 350 cm^{-1}. The a_i parameters for OH stretching modes
318 ranges from -0.9 to 0.1 × 10^{-5} K^{-1} for these humite-group minerals, and the absolute values of a_i parameters
319 are much smaller than those for the lattice and SiO_4 internal modes.

320 According to the model to calculate isochoric heat capacity C_V (Kieffer 1979; Hofmeister 1987; Gillet
321 et al. 1991), the contributions to the macroscopic C_V by a set of m optic continua for different groups of
322 spectroscopic modes is given as:

323 $$C_V = 3nR\sum_{i=1}^{m}\frac{n_i}{N}\int_{x_{li}}^{x_{ui}}\frac{x_i^{\,2}\exp(x_i)\cdot dx_i}{(x_{ui}-x_{li})[\exp(x_i)-1]^2} = 3nR\sum_{i=1}^{m}C_{vi}^{h} \quad (7)$$

324 Where n is the number of atoms in the formula, R is the gas constant, while N is the total number of the
325 vibrational modes. n_i is the number of modes in its continuum with the lower and upper cutoff frequencies
326 of v_{ui} and v_{li}. The variable $x_i = hv_i/kT$, and C_{vi}^{h} is microscopic harmonic heat capacity from the ith
327 vibrational mode. When taking the anharmonic contribution (a_i) at elevated temperatures into consideration,
328 the isochoric heat capacity becomes:

329 $$C_v = 3nR\sum_{i=1}^{m}C_{vi}^{h}\cdot(1-2a_iT) \quad (8)$$

330

331 Based on the spectroscopic data from Lin et al. (2000) and this study, the model of density of states
for OH-clinohumite is derived, and compared with that for forsterite (Gillet et al. 1991) in **Fig. 11(a)**.
332 Totally 191 vibrational modes were calculated for OH-clinohumite (Lin et al. 2000), and the upper and
333 lower cutoff frequencies for each continuum are estimated from the measurements of Lin et al. (2000) and

this study. The internal modes of SiO_4 tetrahedra are classified into 4 groups with the order: v_3 (asymmetric stretching) > v_1 (symmetric stretching) > v_4 (asymmetric bending) > v_2 (symmetric bending), and the ratio between the number of stretching modes (v_1 + v_3) to bending modes (v_2 + v_4) is equal to 4 : 5 (e.g. Hofmeister and et al. 1987). The average a_i for each continuum, calculated in this study, is also listed in the figure.

According to Eqns (7) and (8), we further calculated the harmonic (C_{v_h}) and anharmonic (C_{v_ah}) heat capacities for OH-clinohumite, and comparison is made with those for forsterite (Gillet et al. 1991; Ottonello et al. 2009) in **Fig. 11(b)**. Even when extrapolated to 2000 K, **t**he difference between harmonic and anharmonic capacities is as small as 2 % for clinohumite, while such difference could be up to 7 % for forsterite (Gillet et al. 1991; Ottonello et al. 2009; Yang et al. 2015). It is noted that the harmonic modes for forsterite from Gillet et al. (1991) and Ottonello et al. (2009) agree very well with each other especially above 800 K. In addition, Holland and Powell (1998) modeled the molar isobaric heat capacity (C_P) for clinohumite, as a function of temperature:

$$C_P(kJ\cdot mol^{-1}\cdot K^{-1}) = 1.07 - 1.6533\cdot 10^{-5}\times T - \frac{7.8996\cdot 10^3}{T^2} - \frac{7.3739}{\sqrt{T}} \quad (9)$$

Then the isochoric heat capacity is derived according to the relation below:

$$C_V = C_P - T\cdot V\cdot \alpha^2\cdot K_T \quad (10)$$

The C_V profile for clinohumite based on Eqns (9) and (10) is also plotted in **Fig. 11(b)**, which agrees well with the models from this study, with a relative difference within 2 % up to 2000 K.

4. Implications for DHMS phases

Clinohumite is a potentially abundant Mg-silicate mineral with high water content in subduction zones. Our *in situ* high-temperature FTIR spectra indicate that F-bearing natural clinohumite may survive up to 1243 K without significant dehydration at ambient pressure, whereas the synthetic OH-clinohumite breaks down at 1143 K. In the crystal structure of hydroxyl clinohumite, the hydrogen bonds are elongated due to neighboring H-H repulsion. While such repulsion effect is reduced by F^- substitution ($OH^- = F^-$), and the corresponding H-bonds will become shorter and strengthened. This microscopic phenomenon provides a potential explanation for the possibility that F might stabilize clinohumite to significantly higher temperatures, even above the normal mantle geotherm at low pressure (Engi and Lindsley 1980; Khodyrev et al. 1992; Stalder and Ulmer 2001; Grützner et al. 2017). Moreover, crystal growth evidence in natural samples shows that the F^- substitution may be crucial in stabilizing the crystal structure of the humite minerals by alleviating neighboring H-H repulsion force (Mernagh et al. 1999). This might explain the absence of OH-pure humite minerals in nature (Fujino and Takéuchi 1978). If the H position were fully occupied in an OH-pure clinohumite it would result in an H-H pair with a very short distance, This can be relieved by having a F^- in one half the hydroxyl positions, or by having the M3 position partially occupied by Ti ($Mg^{2+}+2OH^- = Ti^{4+}+2O^{2-}$). In addition, we also identified that the OH-stretching bands at the high frequency range, which correspond to the hydrogen bonds elongated due to neighboring H-H repulsions, show negative temperature dependence, as opposed to the general behaviors of hydrogen bonds in most of hydrous (hydrogen bonded) minerals at high-temperature / high-pressure conditions.

On the other hand, the thermodynamic properties (such as heat capacity) of minerals in the mantle are generally not amenable to experimental tests, since they are unstable at moderate temperatures at low pressure conditions in the laboratory. Then, at high temperature mantle conditions, the heat capacities are typically estimated from the DeBye model for isochoric heat capacity (C_v), which only considers harmonic lattice vibrations (such as in Cynn et al. 1996; Holland and Powell 1998 for many minerals in the mantle). However, the limitations of such quasi-harmonic approximation become severe at high temperature (e.g. Gillet et al. 1991), and the anharmonic contribution must be taken into account (Oganov and Dorogokupets 2004). For example, the heat capacity (C_v) for forsterite is underestimated by up to 7 % in the harmonic model, compared with the more realistic anharmonic model, at the temperature conditions of the upper mantle (Gillet et al. 1991; Yang et al. 2015a). Nevertheless, our study suggests that the DeBye model could

be a reasonable estimation for clinohumite, as a representative of the DHMS phases in the subducting slab, with the anharmonic contributions of no more than 2% at high temperatures in the subduction zone. In addition, the estimated averaged intrinsic anharmonic parameters (a_{i_avg}) for chondrodite and phase A (from **Fig. 10**) are smaller in absolute values, compared with that for forsterite, implying that the anharmonic contributions to the thermodynamic properties in these DHMS phases in the subduction zone could be significantly smaller.

In addition, high-temperature X-ray diffraction experiments further reveal that the DHMS phases which form from dehydration of serpentine in the subducting zones, systematically show larger thermal expansivities than olivine, the most abundant mineral in the upper mantle (e.g. Pawley et al. 1995 for phase A; Ye et al. 2013 and 2015 for clinohumite and chondrodite, respectively; Litasov et al. 2007 and 2008 for superhydrous phase B and phase D, respectively). Potential experiments are still needed for constraints on the thermodynamics as well as elasticity for these DHMS phases, especially at simultaneously high temperature and high pressure conditions, to have a better understanding of the physical properties of the subduction zones.

Acknowledgement: This study was supported by two grants from the National Natural Science Foundation of China (Grant Nos. 41590621 and 41672041) and one grant from the US National Science Foundation Grant (EAR14-16979 to JRS). The electron-microprobe analysis was carried out at the State Key Laboratory of Geological Processes and Mineral Resources, China University of Geosciences (Wuhan); Raman measurements were conducted at the center of Physics Experiment Teaching, University of Science and Technology of China; while FTIR spectra were obtained at Micro-FTIR Laboratory in Department of Earth Sciences, Institute of Geology and Geophysics, Zhejiang University. Many thanks to Zhongqiang Chen, Xinzhuan Guo and Xiang Wu for constructive comments, as well as to to Dr. Zhilei Sui for experimental assistance.

Reference:

Abbott, R.N., Jr, Burnham, C.W., and Post, J.E. (1989) Hydrogen in humite-group minerals: Structure-energy calculations. American Mineralogist, 74, 1300-1306.

Abebe, M., and Walrafen, G.E. (1979) Raman studies of ice VI using a diamond anvil cell. Journal of Chemical Physics, 71, 4167-4169.

Akaogi, M., and Akimoto, S.I. (1980) High pressure stability of a dense hydrous magnesian silicate $Mg_{23}Si_8O_{42}H_6$ and some geophysical implications. Journal of Geophysical Research Solid Earth, 85(B12), 6944-6948.

Balan, E., Refson, K., Blanchard, M., Delattre, S., Lazzeri, M., Ingrin, J., Mauri, F., Wright, K., and Winkler, B. (2008) Theoretical infrared absorption coefficient of OH groups in minerals. American Mineralogist, 93, 950-953.

Berry, A.J., and James, M. (2001) Refinement of hydrogen positions in synthetic hydroxyl-clinohumite by powder neutron diffraction. American Mineralogist, 86(1), 181-184.

Camara, F. (1997) New data on the structure of norbergite; location of hydrogen by X-ray diffraction. Canadian Mineralogist, 35(3), 1523-1530.

Colthup, N.B., Daly, L.H., and Wiberley, S.E. (1964) Introduction to Infrared and Raman Spectroscopy. Academic Press, New York.

Crichton, W.A., and Ross, N.L. (2002) Equation of state of dense hydrous magnesium silicate phase A, $Mg_7Si_2O_8(OH)_6$. American Mineralogist, 87(2-3), 333-338.

Crichton, W.A., and Ross, N.L. (2005) Equations of state of dense hydrous magnesium silicates: results from single-crystal X-ray diffraction. Mineralogical Magazine, 69(3), 273-287.

Cynn, H., Hofmeister, A.M., Burnley, P.C., and Navrotsky, A. (1996) Thermodynamic properties and hydrogen bonding speciation from vibrational spectra of dense hydrous magnesium silicates. Physics and Chemistry of Minerals, 23, 361-376.

Duffy, T.S., Meade, C., Fei, Y., Mao, H.K., and Hemley, R.J. (1995) High-pressure phase transition in brucite, $Mg(OH)_2$. American Mineralogist, 80, 222-230.

Engi, M., and Lindsley, D.H. (1980) Stability of titanian clinohumite: experiments and thermodynamic analysis. Contributions to Mineralogy and Petrology, 72, 1935-1938.

Faust, J., and Knittle, E. (1994) Static compression of chondrodite: Implications for water in the upper

mantle. Geophysical Research Letters, 21(18), 1935-1938.

Friedrich, A., Lager, G.A., Kunz, M., Chakoumakos, B.C., Smyth, J.R., and Schultz, A.J. (2001). American Mineralogist, 86, 981-989.

Friedrich, A., Lager, G.A., Ulmer, P., Kunz, M., and Marshall, W.G. (2002) High-pressure single-crystal X-ray and powder neutron study of F, OH/OD-chondrodite: Compressibility, structure, and hydrogen bonding. American Mineralogist, 87(7), 931-939.

Frost, D.J., and Fei, Y. (1998) Stability of phase D at high pressure and high temperature. Journal of Geophysical Research Solid Earth, 103, 7463-7474.

Frost, R.L., Palmer, S.J., Bouzaid, J.M., and Jagannadha Reddy, B. (2007a) A Raman spectroscopic study of humite minerals. Journal of Raman Spectroscopy, 38(1), 68-77.

Frost, R.L., Palmer, S.J., and Jagannadha Reddy, B. (2007b) Near-infrared and mid-IR spectroscopy of selected humite minerals. Vibrational Spectroscopy, 44(1), 154-161.

Fujino, K., and Takeuchi, Y. (1978) Crystal chemistry of titanian chondrodite and titanian clinohumite of high-pressure origin. American Mineralogist, 63, 535-543.

Gillet, P., Richet, P., Guyot, F., and Fiquet, G. (1991) High-temperature thermodynamic properties of forsterite. Journal of Geophysical Research Solid Earth, 96, 11805-11816.

Grützner, T., Klemme, S., Rohrbach, A., Gervasoni, F., and Berndt, J. (2017) The role of F-clinohumite in volatile recycling processes in subduction zones. Geology 45(5), G38788.1.

Guo, X., and Yoshino, T. (2013) Electrical conductivity of dense hydrous magnesium silicates with implication for conductivity in the stagnant slab. Earth and Planetary Science Letters, 369, 239-247.

Hofmeister, A.M. (1987) Single-crystal absorption and reflection infrared spectroscopy of forsterite and fayalite. Physics and Chemistry of Minerals, 14(6), 499-513.

Hofmeister, A.M., Hoering, T.C., and Virgo, D. (1987) Vibrational spectroscopy of beryllium aluminosilicates: Heat capacity calculations from band assignments. Physics and Chemistry of Minerals, 14(3), 205-224.

Holl, C.M., Smyth, J.R., Manghnani, M.H., Amulele, G.M., Sekar, M., Frost, D.J., Prakapenka, V.B., and Shen, G. (2006) Crystal structure and compression of an iron-bearing Phase A to 33 GPa. Physics and Chemistry of Minerals, 33, 192-199.

Holland, T.J.B., and Powell, R. (1998) An internally consistent thermodynamic data set for phases of petrological interest. Journal of Metamorphic Geology, 16(3), 309-343.

Hushur, A., Manghnani, M.H., Smyth, J.R., Nestola, F., and Frost, D.J. (2009) Crystal chemistry of hydrous forsterite and its vibrational properties up to 41 GPa. American Mineralogist, 94, 751-760.

Irifune, T., Kubo, N., Isshiki, M., and Yamasaki, Y. (1998) Phase transformations in serpentine and transportation of water into the lower mantle. Geophysical Research Letters, 25, 203-206.

Kanzaki, M. (1991) Stability of hydrous magnesium silicates in the mantle transition zone. Physics of the Earth and Planetary Interiors, 66(3-4), 307-312.

Khodyrev, O.Y., Agoshkow, V.M., and Slutsky, A.B. (1992) The system peridotite-aqueous fluid at upper mantle parameters. Transactions (Doklady) of the USSR Academy of Sciences: Earth science sections, 312,255-258.

Kieffer, S.W. (1979) Thermodynamics and lattice vibrations of minerals: 3. Lattice dynamics and an approximation for minerals with application to simple substances and framework silicates. Reviews of Geophysics, 17(1), 35-59.

Kleppe, A.K., Jephcoat, A.P., and Ross, N.L. (2001) Raman spectroscopic studies of phase E to 19 GPa. American Mineralogist, 86(10), 1275-1281.

Kleppe, A.K., Jephcoat, A.P., and Smyth, J.R. (2002) Raman spectroscopic study of hydrous γ-Mg_2SiO_4 to 56.5 GPa. Physics and Chemistry of Minerals, 29, 473-476.

Kleppe, A.K., Jephcoat, A.P., and Smyth, J.R. (2006) High-pressure Raman spectroscopic study of Fo_{90} hydrous wadsleyite. Physics and Chemistry of Minerals, 32, 700-709.

Kuribayashi, T., Kagi, H., Tanaka, M., Akizuki, M., and Kudoh, Y. (2004) High-pressure single-crystal X-ray diffraction and FT-IR observation of natural chondrodite and synthetic OH-chondrodite. Journal of Mineralogical and Petrological Sciences, 99, 118-129.

Kuribayashi, T., Tanaka, M., and Kudoh, Y. (2008) Synchrotron, X-ray analysis of norbergite, $Mg_{2.98}Fe_{0.001}Ti_{0.02}Si_{0.99}O_4(OH)_{0.31}F_{1.69}$ structure at high pressure up to 8.2 GPa. Physics and Chemistry of Minerals, 35, 559-568.

Libowitzky, E. (1999) Correlation of O-H stretching frequencies and O-H...O hydrogen bond lengths in minerals. Monatshefte für Chemie, 130, 1047-1059.

Libowitzky, E., and Rossman, G.R. (1997) An IR absorption calibration for water in minerals. American Mineralogist, 82, 1111-1115.

Lin, C.C., Liu, L.G., and Irifune, T. (1999) High-pressure Raman spectroscopic study of chondrodite. Physics and Chemistry of Minerals, 26(3), 226-233.

Lin, C.C., Liu, L.G., Mernagh, T.P., and Irifune, T. (2000) Raman spectroscopic study of hydroxyl-clinohumite at various pressures and temperatures. Physics and Chemistry of Minerals, 27(5), 320-331.

Litasov, K.D., Ohtani, E., Ghosh, S., Nishihara, Y., Suzuki, A., and Funakoshi, K. (2007) Thermal equation of state of superhydrous phase B to 27 GPa and 1373 K. Physics of the Earth and Planetary Interiors, 164, 142-160.

Litasov, K.D., Ohtani, E., Nishihara, Y., Suzuki, A., and Funakoshi, K. (2008) Thermal equation of state of Al- and Fe-bearing phase D. Journal of Geophysical Research Solid Earth, 113(B8), 8205.

Liu, L.G., Lin, C.C., Mernagh, T.P., and Irifune, T. (1997) Raman spectra of phase A at various pressures and temperatures. Journal of Physics and Chemistry of Solids, 58(12), 2023-2030.

Liu, L.G., Mernagh, T.P., Lin, C.C., Xu, J., and Inoue, T. (1998) Raman spectra of hydrous β-Mg_2SiO_4 at various pressures and temperatures. In: Manghnani MH, Yagi T, Eds., Properties of earth and planetary materials at high pressure and temperature, p.523-530. American Geophysical Union, Washington DC.

Liu, L.G., Lin, C.C., and Mernagh, T.P. (1999) Raman spectra of norbergite at various pressures and temperatures. European Journal of Mineralogy, 11(6), 1011-1021.

Liu, Z.X., Lager, G.A., Hemley, R.J., and Ross, N.L. (2003) Synchrotron infrared spectroscopy of OH-chondrodite and OH-clinohumite at high pressure. American Mineralogist, 88(10), 1412-1415.

Liu, P.L. (2015) UHP impure marbles from Ganjialing, Dabie mountains: metamorphic evolution and carbon cycling in continental subduction zones, 31 p. Ph.D. thesis, China University of Geosciences (Wuhan).

McGetchin, T.R., Silver, L.T., and Chodos A.A. (1970) Titanoclinohumite: A possible mineralogical site for water in the upper mantle. Journal of Geophysical Research Solid Earth, 75(75), 255-259.

Mernagh, T.P., Liu, L.G., and Lin, C.C. (1999) Raman spectra of chondrodite at various temperatures.

Journal of Raman Spectroscopy, 30(10), 963-969.

Oganov, A.R. and Dorogokupets P.I. (2004) Intrinsic anharmonicity in equations of state and thermodynamics of solids. Journal of Physics: Condensed Matter, 16, 1351-1360.

Ohtani, E., Toma, M., Litasov, K., Kubo, T., and Suzuki, A. (2001) Stability of dense hydrous magnesium silicate phases and water storage capacity in the transition zone and lower mantle. Physics of the Earth and Planetary Interiors, 124, 105-117.

Okada, T., Narita, T., Nagai, T., and Yamanaka, T. (2008) Comparative Raman spectroscopic study on ilmenite-type $MgSiO_3$ (akimotoite), $MgGeO_3$, and $MgTiO_3$ (geikielite) at high temperatures and high pressures. American Mineralogist, 93(1), 39-47.

Ottolini, L., Cámara, F., and Bigi, S. (2000) An investigation of matrix effects in the analysis of fluorine in humite-group minerals by EMPA, SIMS, and SREF. American Mineralogist, 85(1), 89-102.

Ottonello, G., Civalleri, B., Ganguly, J., Zuccolini, M.V., and Noel, Y. (2009) Thermophysical properties of the α–β–γ polymorphs of Mg_2SiO_4 : a computational study. Physics and chemistry of Minerals, 36(2), 87-106.

Paterson, M.S. (1982) The determination of hydroxyl by infrared absorption in quartz, silicate glasses and similar materials. Bull Mineral, 105(1), 20-29.

Pawley, A.R., Redfern, S.A.T., and Wood, B.J. (1995) Thermal expansivities and compressibilities of hydrous phases in the system MgO-SiO_2-H_2O: talc, phase A and 10-Å phase. Contributions to Mineralogy and Petrology, 122, 301-307.

Prasad, P.S.R., and Sarma, L.P. (2004) A near-infrared spectroscopic study of hydroxyl in natural chondrodite. American Mineralogist, 89, 1056-1060.

Qin, F., Wu, X., Zhang D., Qin, S., and Jacobsen, S.D. (2017) Thermal equation of state of natural Ti-bearing clinohumite. Journal of Geophysical Research Solid Earth 122(11).

Ribbe, P.H. (1979) Titanium, fluorine, and hydroxyl in the humite minerals. American Mineralogist, 64, 1027-1035.

Ribbe, P.H., and Gibbs, G.V. (1988) Crystal structures of the humite minerals: III. Mg/Fe ordering in humite and its relation to other ferromagnesian silicates. American Mineralogist, 56, 1155-1173.

Robinson, K., Gibbs, G.V., and Ribbe, P.H. (1973) The crystal structure of the humite minerals IV.

548 Clinohumite and Titanoclinohumite. American Mineralogist, 58, 43-49.

549 Ross, N.L., and Crichton, W. (2001) Compression of synthetic hydroxylclinohumite [$Mg_9Si_4O_{16}(OH)_2$] and
550 hydroxylchondrodite[$Mg_5Si_2O_8(OH)_2$]. American Mineralogist, 86(8-9), 990-996.

551 Sánchez-Viscaino, V.L., Trommsdorff, V., Gómez-Pugnaire, M.T., Garrido, C.J., Müntener, O., and
552 Connolly, J.A.D. (2005) Petrology of titanian clinohumite and olivine at the high-pressure breakdown
553 of antigorite serpentinite to chlorite harzburgite. Contributions to Mineralogy and Petrology, 149,
554 627-646.

555 Shen, T., Hermann, J., Zhang, L., Padrón-Navarta, J.A., and Chen, J. (2014) FTIR spectroscopy of
556 Ti-chondrodite, Ti-clinohumite, and olivine in deeply subducted serpentinites and implications for the
557 deep water cycle. Contributions to Mineralogy and Petrology, 167(4), 1-15.

558 Shen, T., Hermann, J., Zhang, L., Lü, Z., Padrón-Navarta, J.A., Xia, B., and Bader, T. (2015) UHP
559 metamorphism documented in Ti-chondrodite- and Ti-clinohumite- bearing serpentinized ultramafic
560 rocks from Chinese southwestern Tianshan. Journal of petrology, 56(7), 1425-1458.

561 Shieh, S.R., Duffy, T.S., Liu, Z., and Ohtani, E. (2009) High-pressure infrared spectroscopy of the dense
562 hydrous magnesium silicates phase D and phase E. Physics of the Earth and Planetary Interiors, 175,
563 106-114.

564 Sinogeikin, S.V., and Bass, J.D. (1999) Single-crystal elastic properties of chondrodite: implications for
565 water in the upper mantle. Physics and Chemistry of Minerals, 26(4), 297-303.

566 Smyth, J.R., Holl, C.M., Frost, D.J., and Jacobsen, S.D. (2004) High pressure crystal chemistry of hydrous
567 ringwoodite and water in the Earth's interior. Physics of the Earth and Planetary Interiors,
568 143,271-278.

569 Smyth, J.R., Frost, D.J., and Nestola, F. (2005) Hydration of olivine and the Earth's deep water cycle.
570 Geochimica et Cosmochimica Acta Supplement, 69, Supplement 1, Goldschmidt Conference
571 Abstracts, p. A746.

572 Smyth, J.R., Frost, D.J., Nestola, F., Holl, C.M., and Bromiley, G. (2006) Olivine hydration in the deep
573 upper mantle: Effects of temperature and silica activity. Geophysical Research Letters, 33(15),
574 311-324.

575 Stalder, R., and Ulmer, P. (2001) Phase relations of a serpentine composition between 5 and 14 GPa:

significance of clinohumite and phase E as water carriers into the transition zone. Contributions to Mineralogy and Petrology, 140, 670-679.

Suzuki, S., and Nakashima, S. (1999) In-situ IR measurements of OH species in quartz at high temperatures. Physics and Chemistry of Minerals, 26, 217–225.

Walrafen, G.E., Abebe, M., Mauer, F.A., Block, S., Piermarini, G.J., and Munro, R. (1982) Raman and X-ray investigations of ice VII to 36.0 GPa. Journal of Chemical Physics, 77, 2166-2174.

Williams, Q. (1992) A vibrational spectroscopic study of hydrogen in high pressure mineral assemblages. In: Syono Y. and Manghnani M. H., Eds., Geophysical Monograph Series, 67, p. 289-296. American Geophysical Union, Washington, D. C.

Wunder, B. (1998) Equilibrium experiments in the system $MgO–SiO_2–H_2O$ (MSH): stability fields of clinohumite-OH [$Mg_9Si_4O_{16}(OH)_2$], chondrodite-OH [$Mg_5Si_2O_8(OH)_2$] and phase A ($Mg_7Si_2O_8(OH)_6$). Contributions to Mineralogy and Petrology, 132(2), 111-120.

Wunder, B., Medenbach, O., Daniels, P., and Schreyer, W. (1995) Letters. First synthesis of the hydroxyl end-member of humite, $Mg_7Si_3O_{12}(OH)_2$. American Mineralogist, 80(7-8), 638-640.

Yamamoto, K., and Akimoto, S. (1977). The system $MgO-SiO_2-H_2O$ at high pressures and temperatures stability field for hydroxyl-chondrodite, hydroxyl-clinohumite and 10 Å-phase. American Journal of Science 277, 288-312.

Yang, X.Z., Keppler, H., Dubrovinsky, L., and Kurnosov, A. (2014) In-situ infrared spectra of hydroxyl in wadsleyite and ringwoodite at high pressure and high temperature. American Mineralogist, 99, 724-729.

Yang, Y., Xia, Q.K., Feng, M., and Zhang, P.P. (2010) Temperature dependence of IR absorption of OH species in clinopyroxene. American Mineralogist 95(10), 1439-1443.

Yang, Y., Wang, Y., Smyth, J.R., Liu, J., and Xia, Q.K. (2015a) Water effects on the anharmonic properties of forsterite. American Mineralogist, 100(10), 2185-2190.

Yang, Y., Xia, Q.K., and Zhang, P.P. (2015b) Evolution of OH groups in diopside and feldspars with temperature. European Journal of Mineralogy, 27(2), 185-192.

Ye, Y., Schwering, R.A., and Smyth, J.R. (2009) Effects of hydration on thermal expansion of forsterite, wadsleyite, and ringwoodite at ambient pressure. American Mineralogist, 94, 899-904.

Ye, Y., Smyth, J.R., Jacobsen, S.D., and Goujon, C. (2013) Crystal chemistry, thermal expansion, and Raman spectra of hydroxyl-clinohumite: implications for water in Earth's interior. Contributions to Mineralogy and Petrology, 165(3), 563-574.

Ye, Y., Jacobsen, S.D., Mao, Z., Duffy, T.S., Hirner, S.M., and Smyth, J.R. (2015) Crystal structure, thermal expansivity, and elasticity of OH-chondrodite: trends among dense hydrous magnesium silicates. Contributions to Mineralogy and Petrology, 169(4), 43.

Zhang, M., Salje, E.K.H., Carpenter, M.A., Wang, J.Y., Groat, L.A., Lager, G.A., Wang, L., Beran, A., and Bismayer, U. (2007) Temperature dependence of IR absorption of hydrous/hydroxyl species in minerals and synthetic materials. American Mineralogist, 92, 1502-1517.

Zhang, R.X., and Yang, S.Y. (2016) A mathematical model for determining carbon coating thickness and its application in electron probe microanalysis. Microscopy and Microanalysis, 22(6), 1374-1380.

Zheng, Y.F. (2012) Metamorphic chemical geodynamics in continental subduction zones. Chemical Geology, 328(7420), 5-48.

Figure captions:

Fig. 1 Sketch of the crystal structure of OH-clinohumite viewed approximately down in *a* direction. The two proton positions are shown as small white spheres, and the covalent OH bands are presented as black short lines.

Fig. 2 Raman spectra of the natural and synthetic samples at 300 K, with the peak positions labeled and the background subtracted.

Fig. 3 Selected Raman spectra of natural **(a)** and synthetic **(b)** clinohumite at elevated temperatures, with the background subtracted.

Fig. 4 Temperature dependence of Raman bands shifts for both the natural (black circles) and synthetic (gray diamond) clinohumite samples with linear regressions in black and gray lines, respectively, in the frequency ranges of **(a)** 100-400 cm^{-1}, **(b)** 400-800 cm^{-1}, **(c)** 800-1000 cm^{-1}. The peak positions at 300 K are labeled in the figures.

Fig. 5 FTIR spectra of the natural and synthetic clinohumite at 300 K, with the peak positions labeled.

Fig. 6 Schematic illustrations of the variation of the H position in OH-clinohumite at both ambient **(a)** and **(b)** high temperatures (after Lin et al. 2000). The dotted lines denote the hydrogen bonds, while the solid lines represent covalent bonds. The equilibrium angles (θ_1 and θ_2) are the intersection angles between OH groups and [001] direction for the space group of $P2_1/b$. Both angles are nearly the same at 300 K, while θ_1 becomes smaller at elevated temperatures, without any significant variation in θ_2.

Fig. 7 Selected IR spectra of natural **(a)** and synthetic **(b)** clinohumite samples at high temperatures.

Fig. 8 Temperature dependence of OH-stretching bands frequencies at atmospheric pressure for both the natural (black circles) and synthetic (gray diamond) clinohumite samples with linear regressions. The frequencies of OH band at room temperatures are listed in the figures.

Fig. 9 The isobaric **(a)** and isothermal **(b)** mode Grüneisen parameters for the hydrous silicate phases, calculated from the Raman measurements at high temperature (this study for clinohumite samples; Mernagh et al. 1999 for chondrodite; Liu et al. 1997 for phase A; Yang et al. 2015 for hydrous forsterite) and high pressure (Lin et al. 2000 for clinohumite; Lin et al. 1999 for chondrodite; Liu et al. 1997 for phase A; Hushur et al. 2009 for hydrous forsterite).

653

654 **Fig. 10** Variation of the intrinsic anharmonic parameters (a_i) with frequency for clinohumite, chondrodite,
655 phase A, and hydrous fortertie.

656

657 **Fig. 11 (a)** Models of density of states for OH-clinohumite (This study) and forsterite (Gillet et al. 1991).
658 The boxes denote the continua for different spectroscopic modes (without acoustic modes). The numbers
659 inside and above each box represent the number of modes and the mean a_i parameter, respective, in that
660 continuum. The upper and lower cutoff frequencies for each continuum are also labeled below the box.
661 External modes are T (translation) and R (rotation), while internal modes for SiO_4 tetrahedra are denoted as
662 ν_1, ν_3 (stretching vibrations) and ν_2, ν_4 (bending vibrations). **(b)** Comparison of the heat capacities (C_V) for
663 clinohumite and forsterite ((Gillet et al. 1991; Ottonello et al. 2009).

664

665 **Table 1.** Electron microprobe analyses for the natural clinohumite sample

Weight percent (wt%)			apfu
FeO	6.51(1)	Fe	0.582(8)
MgO	49.14(5)	Mg	7.842(9)
CaO	0.015(7)	Ca	0.001(8)
MnO	0.130(2)	Mn	0.011(8)
Al_2O_3	0.020(1)	Al	0.002(5)
TiO_2	3.10(8)	Ti	0.250(2)
NiO	0.020(9)	Ni	0.001(8)
SiO_2	37.36 (7)	Si	4
F	0.59(6)	F	0.201(7)

This is a preprint, the final version is subject to change, of the American Mineralogist (MSA)
Cite as Authors (Year) Title. American Mineralogist, in press.
DOI: https://doi.org/10.2138/am-2019-6604

Cl	0.005(6)	Cl	0.001(1)
H_2O^{a}	1.82	H	1.296(8)
Total	98.74		

a: The weight percentage values for H_2O are calculated from stoichiometry, and the mole ratio of (H+F+1/2·Ti) : O is assumed to be 2 : 18, considering the substitutions of $OH^-=F^-(Cl^-)$ and $Mg^{2+}+2OH^-=Ti^{4+}+2O^{2-}$.

Table 2. The observed Raman shifts and OH bands by FTIR (ν_i), temperature dependence of ν_i ($\partial\nu_i/\partial T$), isobaric mode Grüneisen parameters, as well as intrinsic anharmonic parameters (a_i) for the clinohumite samples

Natural clinohumite			Synthetic clinohumite				
ν_i (cm^{-1})	$(\partial\nu_i/\partial T)_P$ ($cm^{-1}K^{-1}$)	γ_{iP}	ν_i (cm^{-1})	$(\partial\nu_i/\partial T)_P$ ($cm^{-1}K^{-1}$)	γ_{iP}	γ_{iT}^{a}	a_i ($10^{-5}K^{-1}$)
133	-0.004(3)	0.92(7)	142	-0.013(9)	2.65(4)		
			183	-0.013(6)	2.01(3)		
206	-0.006(8)	0.94(7)	208	-0.006(4)	0.83(4)	1.769	3.44(8)
233	-0.014(3)	1.75(6)	227	-0.005(7)	0.68(2)		
264	-0.025	2.71(3)	268	-0.017(7)	1.79(4)		
			307	-0.034(7)	3.06(9)		
321	-0.015(3)	1.36(5)	326	-0.022(1)	1.83(7)	1.221	-2.27
352	-0.021(8)	1.77(7)	363	-0.004(5)	0.33(6)		

This is a preprint, the final version is subject to change, of the American Mineralogist (MSA)
Cite as Authors (Year) Title. American Mineralogist, in press.
DOI: https://doi.org/10.2138/am-2019-6604

384	-0.021(4)	1.59(6)	378	-0.030(9)	2.21(7)	0.861	-4.99(7)
			429	-0.023(1)	1.46(1)	1.142	-1.17(4)
532	-0.027(2)	1.46(6)	549	-0.015	0.74(1)	0.815	0.27
			587	-0.014(6)	0.67(5)	0.484	-0.70(6)
603	-0.011(5)	0.54(6)	603	-0.018(4)	0.82(7)	0.596	-0.85(1)
651	-0.019(1)	0.84(1)					
691	-0.017(4)	0.72(1)					
755	-0.01	0.38	744	0.00004	-0.001	0.355	1.31(5)
780	-0.014(8)	0.54(4)	777	-0.04(5)	1.57(1)	0.355	-4.48(2)
830	-0.019(1)	0.66	832	-0.008(1)	0.26(4)	0.357	0.34(1)
842	-0.014(7)	0.50(1)	842	-0.012(7)	0.40(9)	0.317	-0.33(8)
861	-0.021(3)	0.70(9)	861	-0.020(2)	0.63(6)	0.366	-0.99(6)
928	-0.015(1)	0.46(6)	933	-0.025	0.72(7)	0.362	-1.34(4)
965	-0.028(1)	0.83(4)	969	-0.028(6)	0.80(1)	0.670	-0.48
3309	0.015(8)	-0.13(7)					
3397	0.021(8)	-0.18(4)					
3529	-0.027(6)	0.22(4)	3526	-0.023	0.180	0.016	-0.60(4)
3564	-0.022(9)	0.18(4)	3560	-0.028	0.21(3)	0.039	-0.64(2)
3608	-0.041(7)	0.33(1)	3609	-0.046	0.34(3)		

673 ***a***: Lin et al. (2000)

674

This is a preprint, the final version is subject to change, of the American Mineralogist (MSA)
Cite as Authors (Year) Title. American Mineralogist, in press.
DOI: https://doi.org/10.2138/am-2019-6604

Table 3. Observed IR modes for both the natural and synthetic clinohumite samples in bold, compared with the literature in the frequency range of 3100-3650 cm^{-1}.

Below 3450 cm^{-1}				above 3450 cm^{-1}					method
F-free:									
				3526		3560		3608	IR[a]
				3522		3560	3575	3608	Raman[b]
				3526		3561		3607	IR[c]
				3524	3544	3557	3567	3576	IR[d]
				3527	3535	3559	3568	3578	Raman[e]
				3527			3564	3580 3612	Raman[f]
F-bearing:									
3161	3233	3397	3436	3529		3564		3608	IR[a]
		3393		3525		3562			IR[g]

a: this study; ***b***: Ye et al. (2013); ***c***: Liu et al. (2003); ***d***: Frost et al. (2007b); ***e***: Frost et al. (2007a); ***f***: Lin et al. (2000); ***g***: Shen et al. (2014).

Table 4. Comparison of some hydrogen bonds from FTIR measurement and neutron powder diffraction for hydroxyl-clinohumite.

OH band (cm-1) [a]	$d_{O...H}$ (Å) [b]	$d_{O...D}$ (Å) [c]
3526	2.09	2.01 (O9...D1)
3560	2.17	2.23 (O8...D2)
3609	2.42	2.46 (O6...D1)

a: measured by FTIR in this study; ***b***: calculated from Equation (1) (Libowitzky 1999); ***c***: measured by neutron powder diffraction (Berry and James 2001).

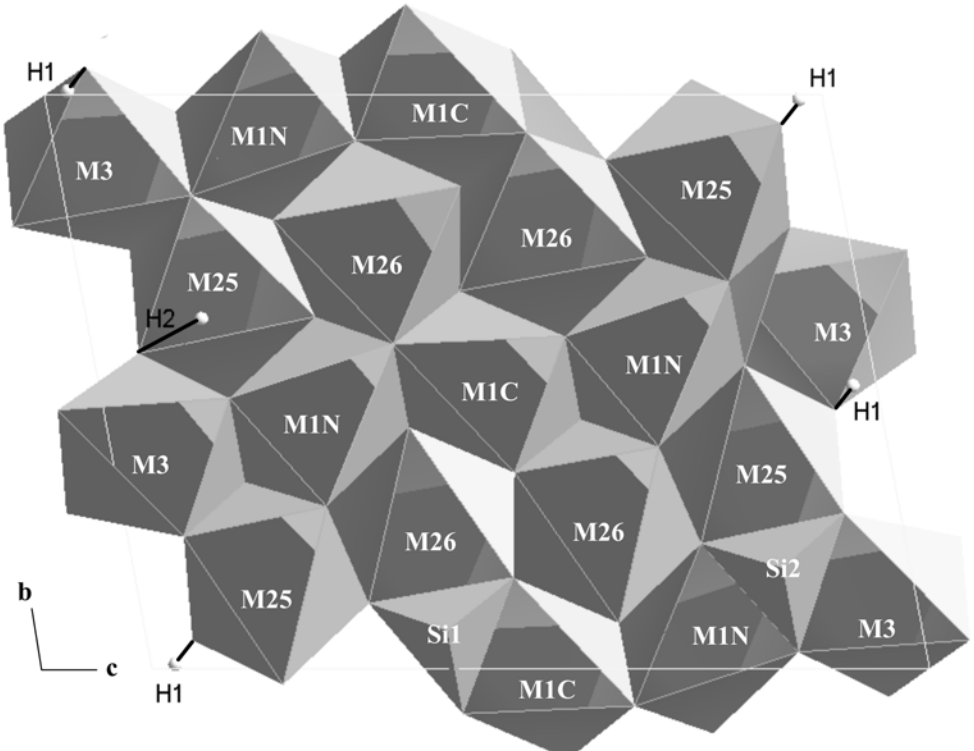
H1
M3
M1N
M1C
H1
M25
M26
M25
H2
M26
M3
M1N
M1C
H1
M3
M1N
M25
M26
M26
Si2
M25
Si1
M1N
M3
M1C
H1
b
c

Fig. 1

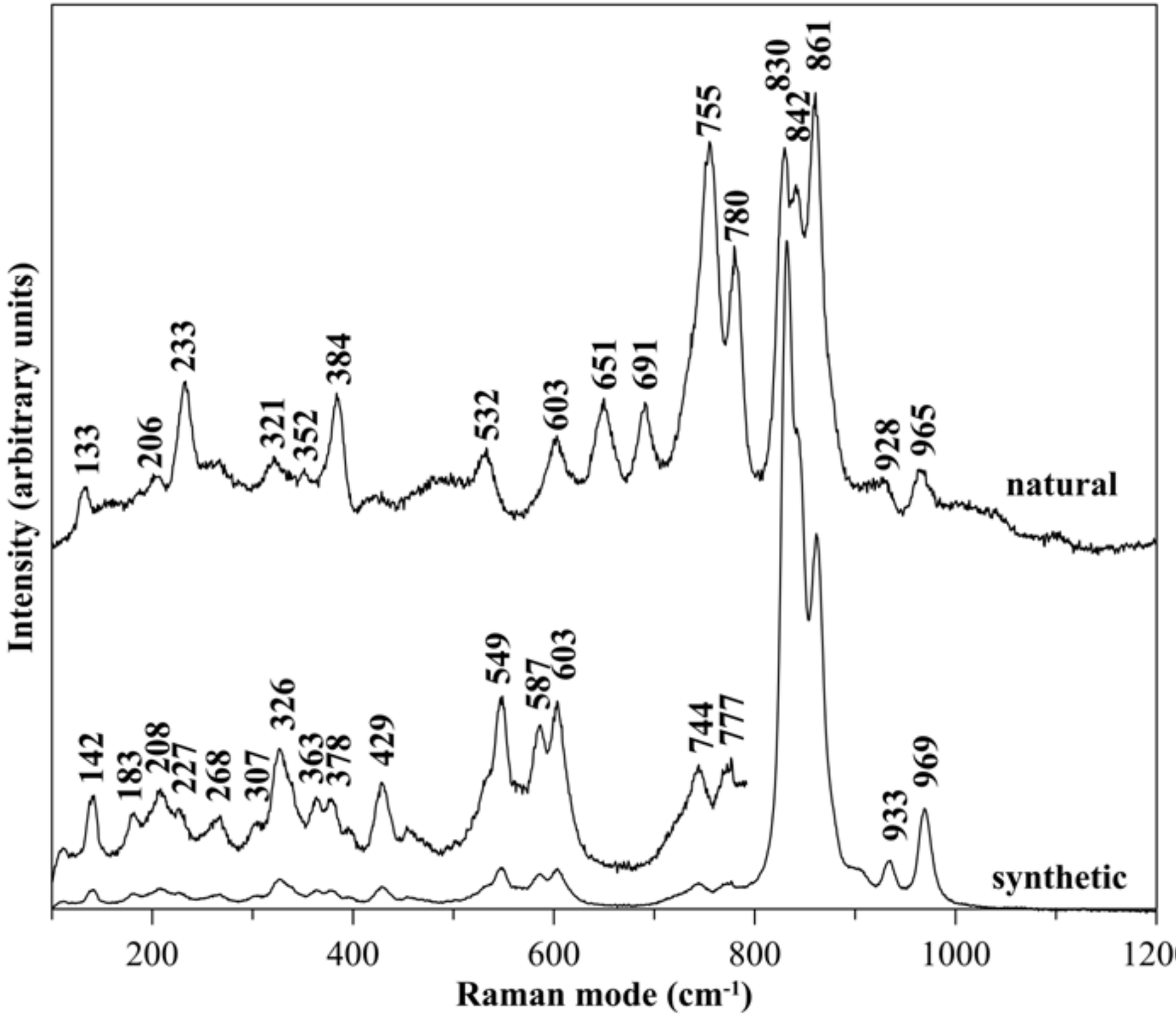
Intensity (arbitrary units)
Raman mode (cm-1)
200
400
600
800
1000
1200
natural
synthetic
133
206
233
321
352
384
532
603
651
691
755
780
830
842
861
928
965
142
183
208
227
268
307
326
363
378
429
549
587
603
744
777
933
969

Fig. 2

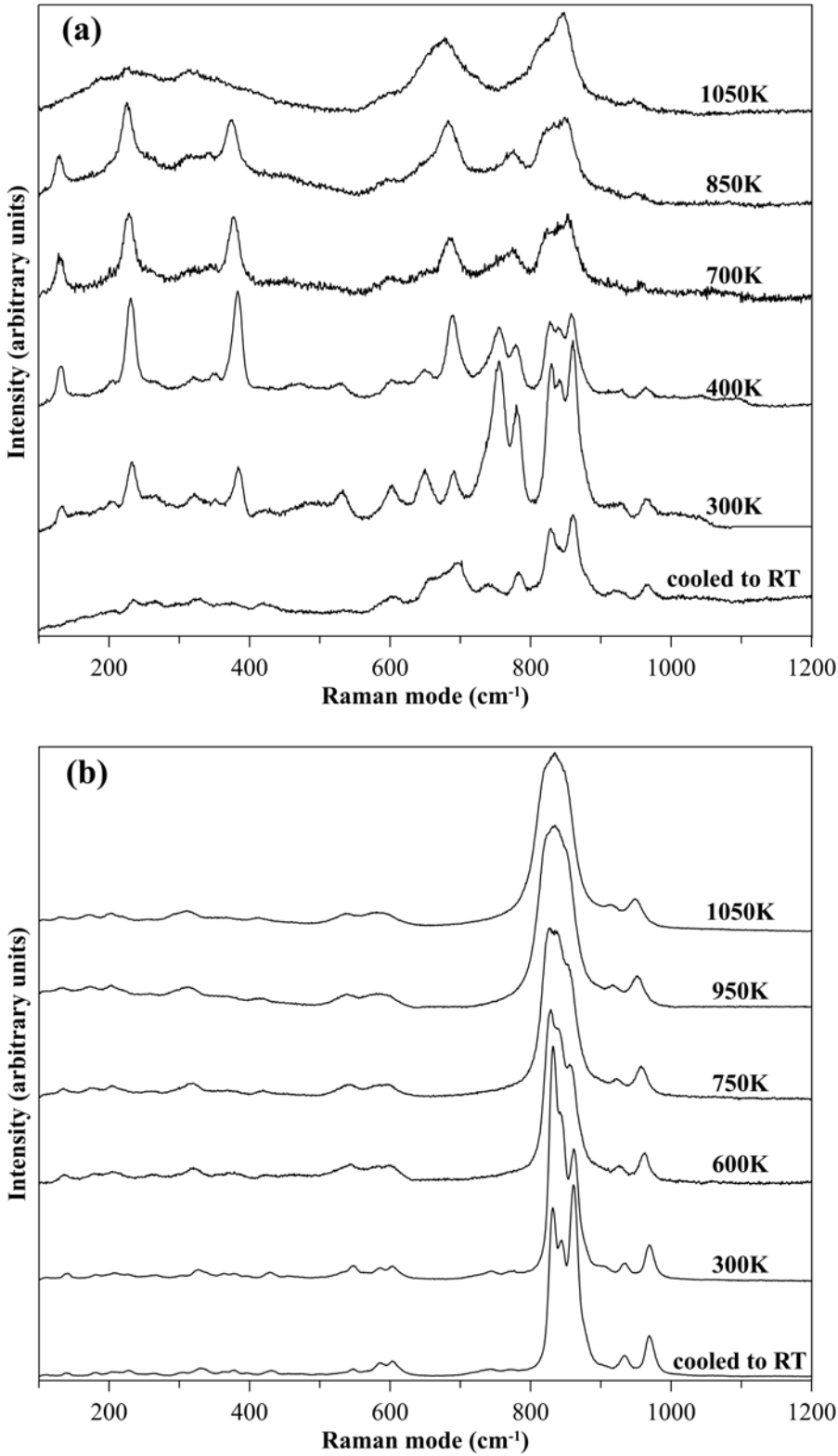
(a)
1050K
850K
700K
400K
300K
cooled to RT
Intensity (arbitrary units)
200
400
600
800
1000
1200
Raman mode (cm-1)
(b)
1050K
950K
750K
600K
300K
cooled to RT
Intensity (arbitrary units)
200
400
600
800
1000
1200
Raman mode (cm-1)

Fig. 3

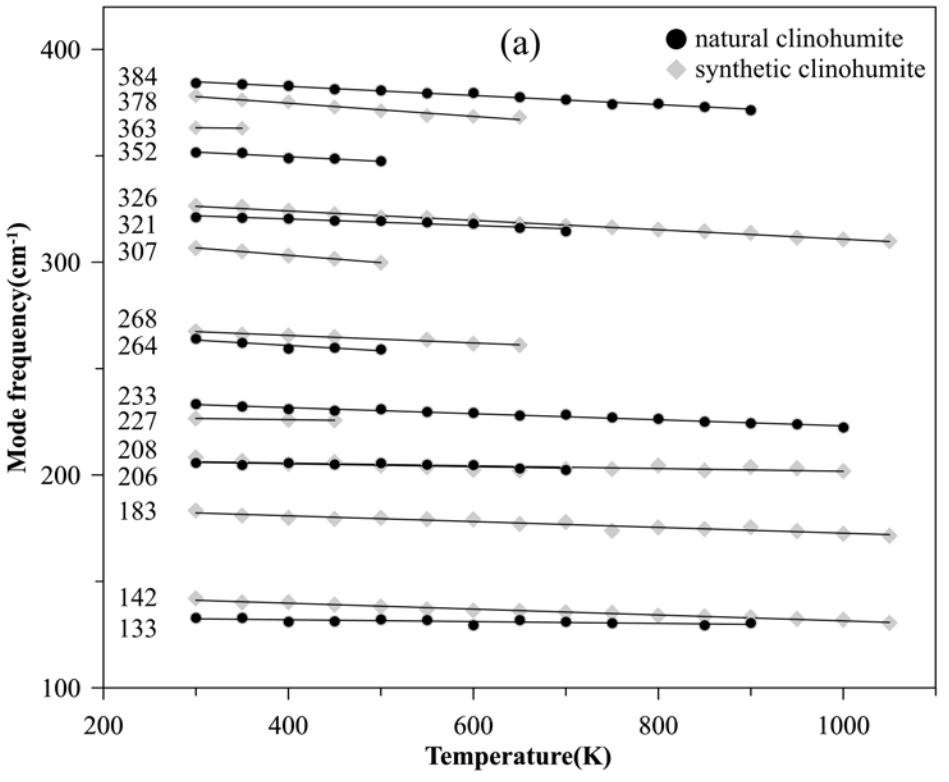
(a)
natural clinohumite
synthetic clinohumite
384
378
363
352
326
321
307
268
264
233
227
208
206
183
142
133
Mode frequency(cm-1)
Temperature(K)

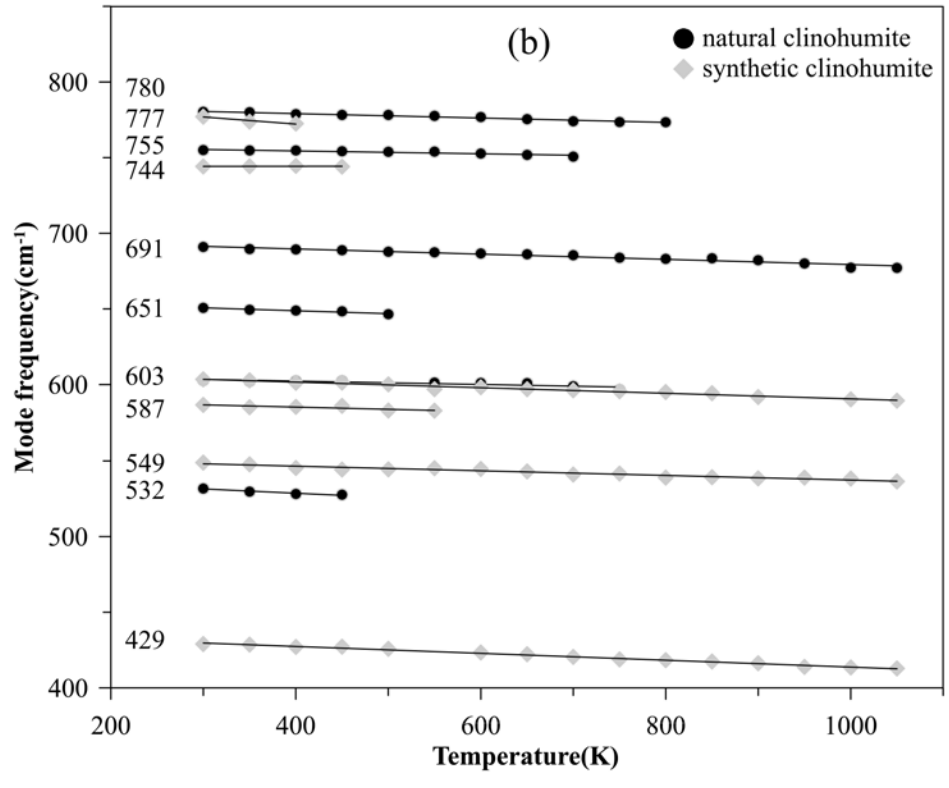
(b)
natural clinohumite
synthetic clinohumite
780
777
755
744
691
651
603
587
549
532
429
Mode frequency(cm-1)
Temperature(K)

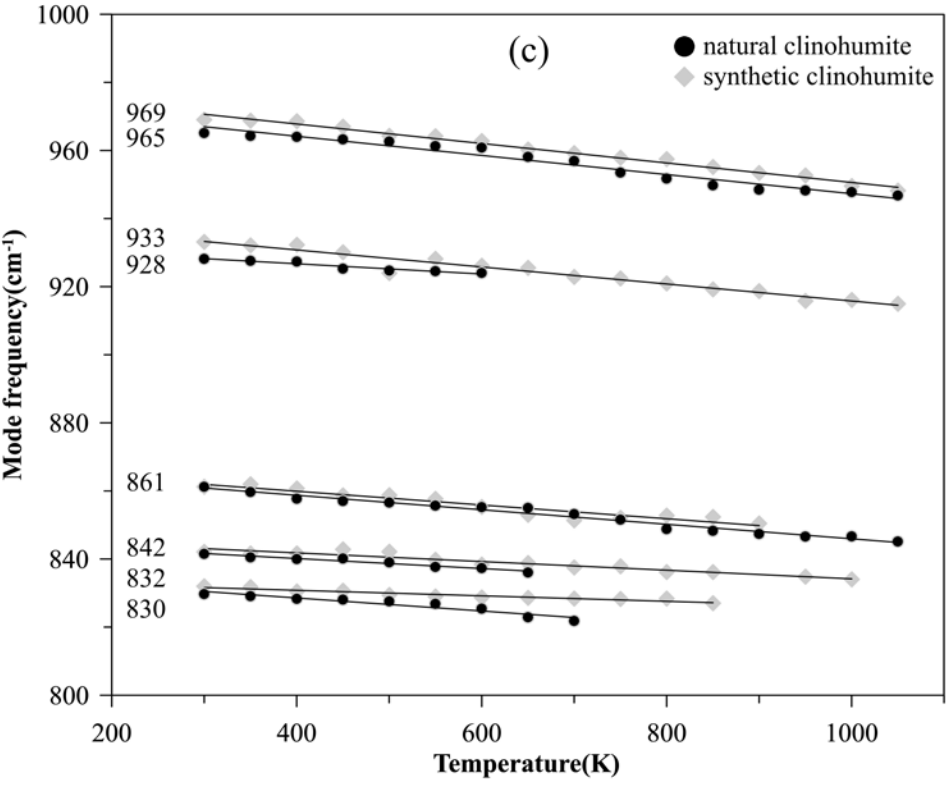
(c)
natural clinohumite
synthetic clinohumite
969
965
933
928
861
842
832
830
Mode frequency(cm-1)
Temperature(K)

Fig. 4

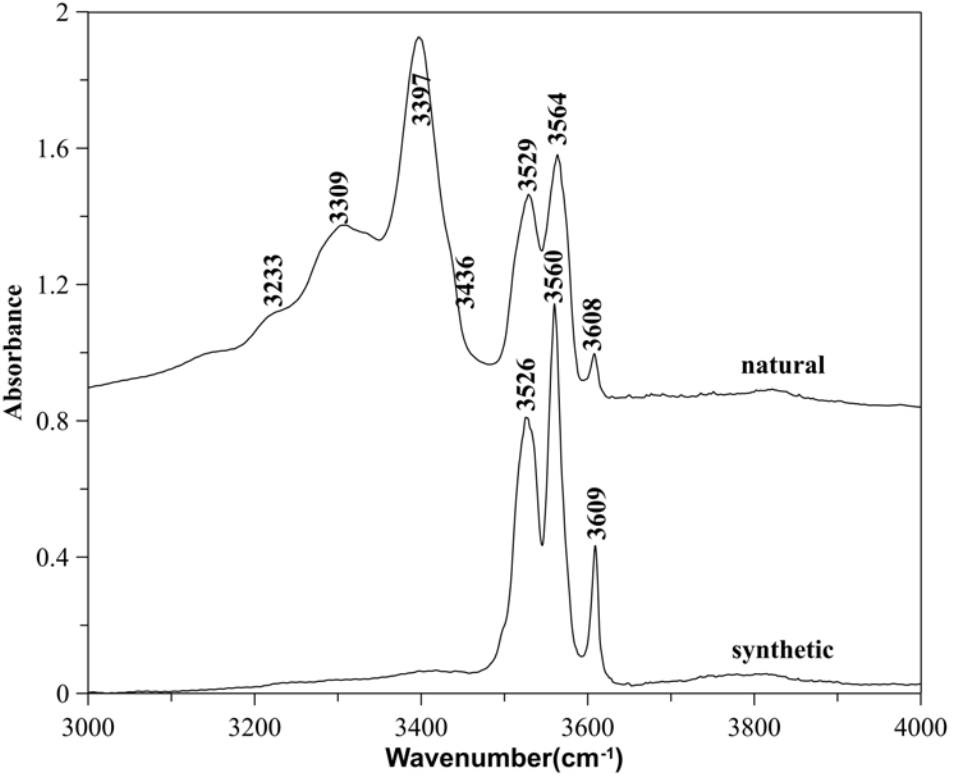
Absorbance
Wavenumber(cm-1)
natural
synthetic
3233
3309
3397
3436
3529
3564
3560
3608
3526
3609

Fig. 5

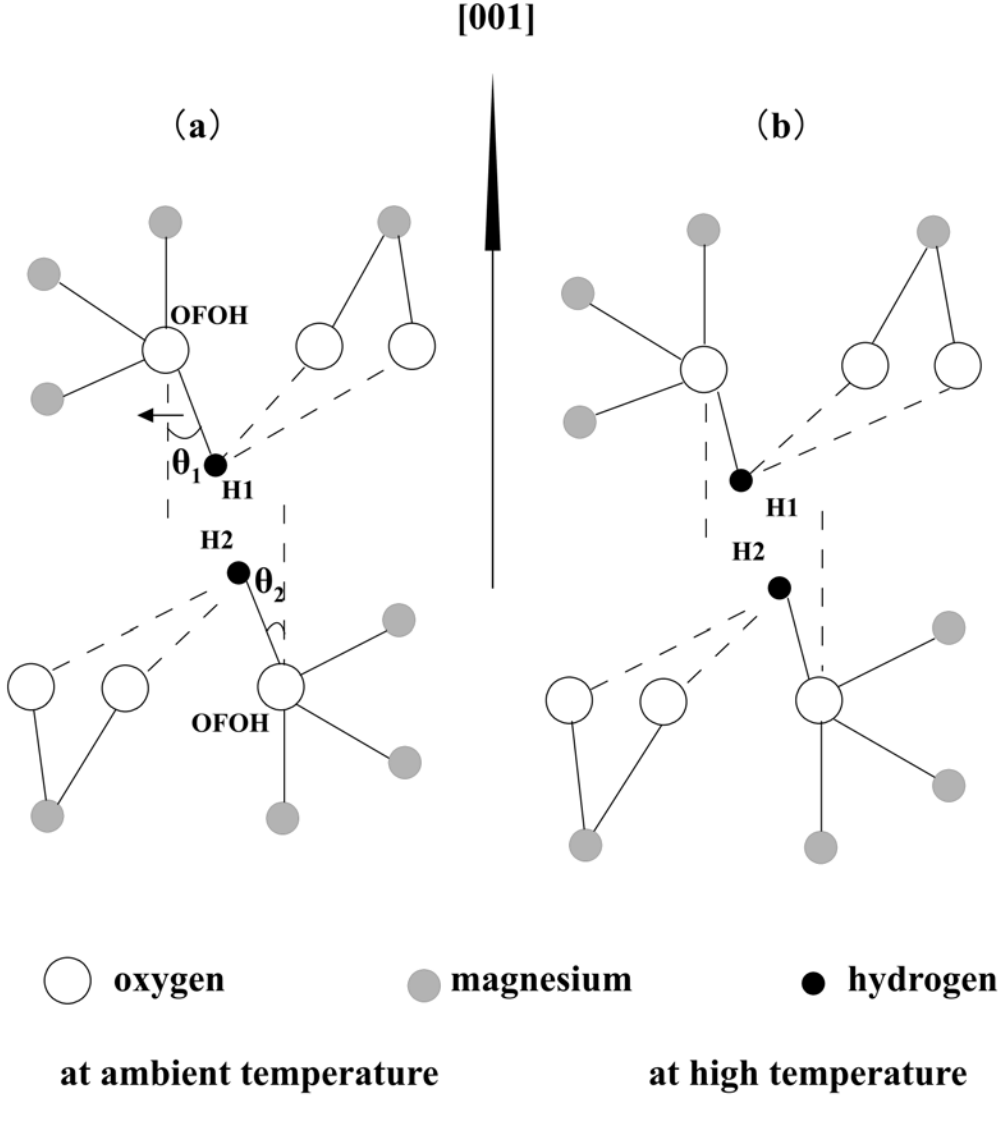
[001]
(a)
(b)
OFOH
θ1
H1
H2
θ2
OFOH
H1
H2
oxygen
magnesium
hydrogen
at ambient temperature
at high temperature

Fig. 6

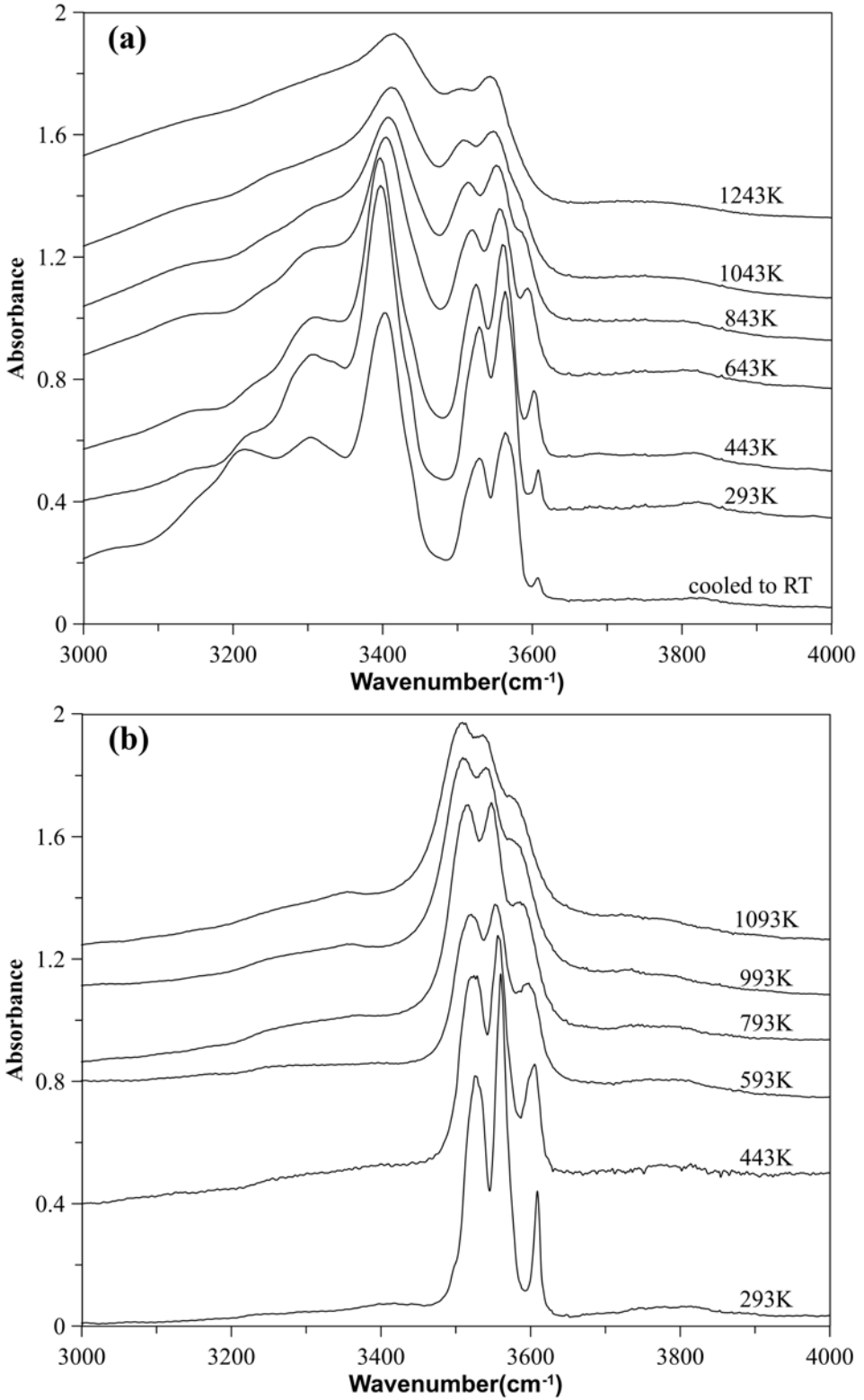
(a)
Absorbance
Wavenumber(cm-1)
1243K
1043K
843K
643K
443K
293K
cooled to RT
(b)
Absorbance
Wavenumber(cm-1)
1093K
993K
793K
593K
443K
293K

Fig. 7

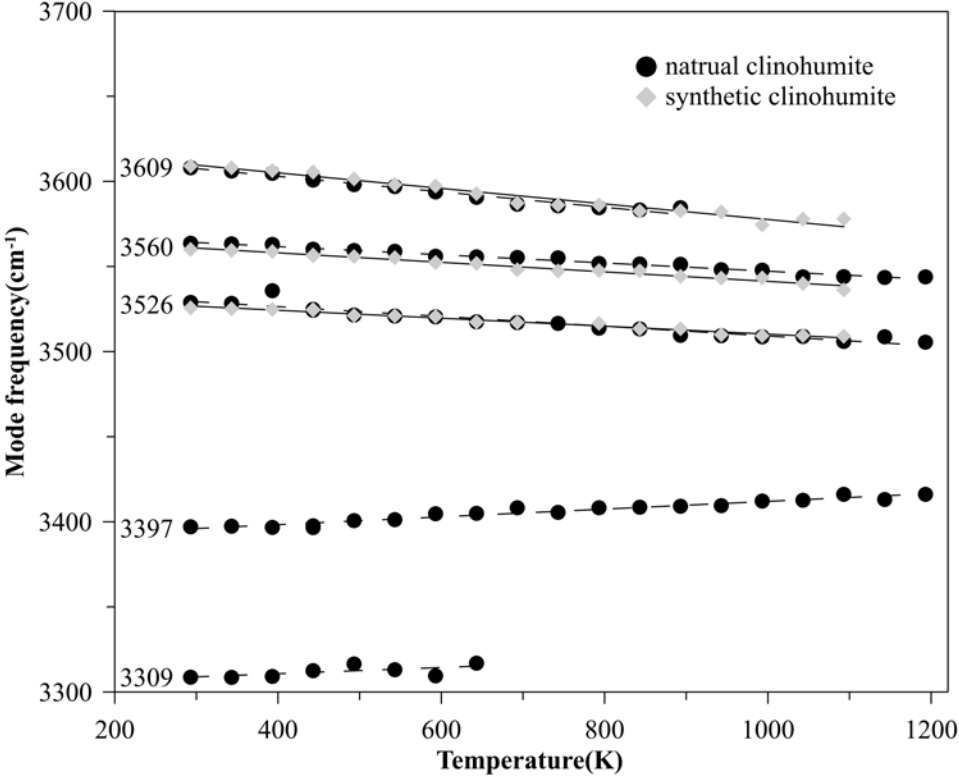
natrual clinohumite
synthetic clinohumite
3609
3560
3526
3397
3309
Mode frequency(cm-1)
Temperature(K)
3700
3600
3500
3400
3300
200
400
600
800
1000
1200

Fig. 8

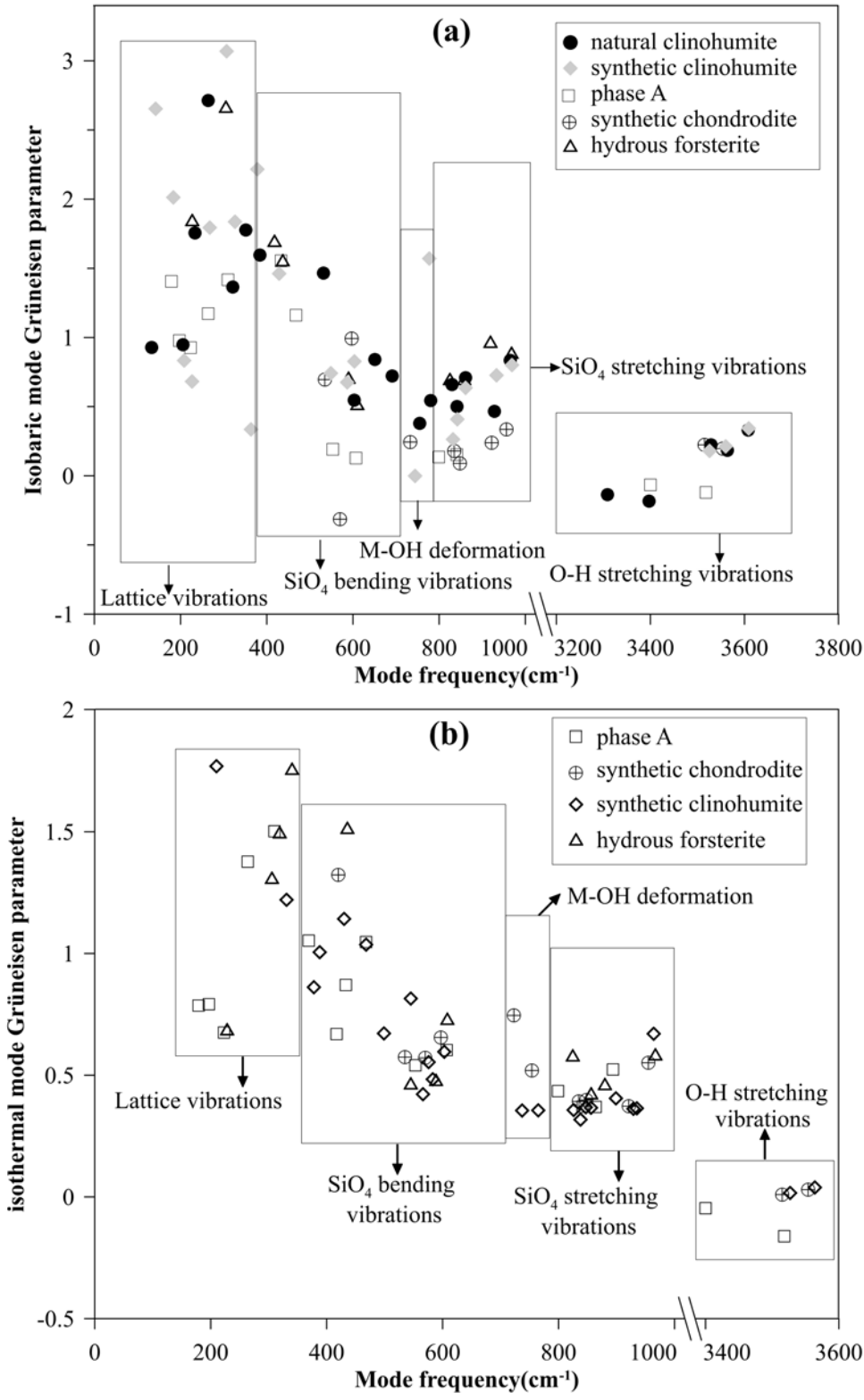
(a)
natural clinohumite
synthetic clinohumite
phase A
synthetic chondrodite
hydrous forsterite
Isobaric mode Grüneisen parameter
SiO4 stretching vibrations
M-OH deformation
SiO4 bending vibrations
Lattice vibrations
O-H stretching vibrations
Mode frequency(cm-1)
(b)
phase A
synthetic chondrodite
synthetic clinohumite
hydrous forsterite
isothermal mode Grüneisen parameter
M-OH deformation
Lattice vibrations
SiO4 bending vibrations
SiO4 stretching vibrations
O-H stretching vibrations
Mode frequency(cm-1)

Fig. 9

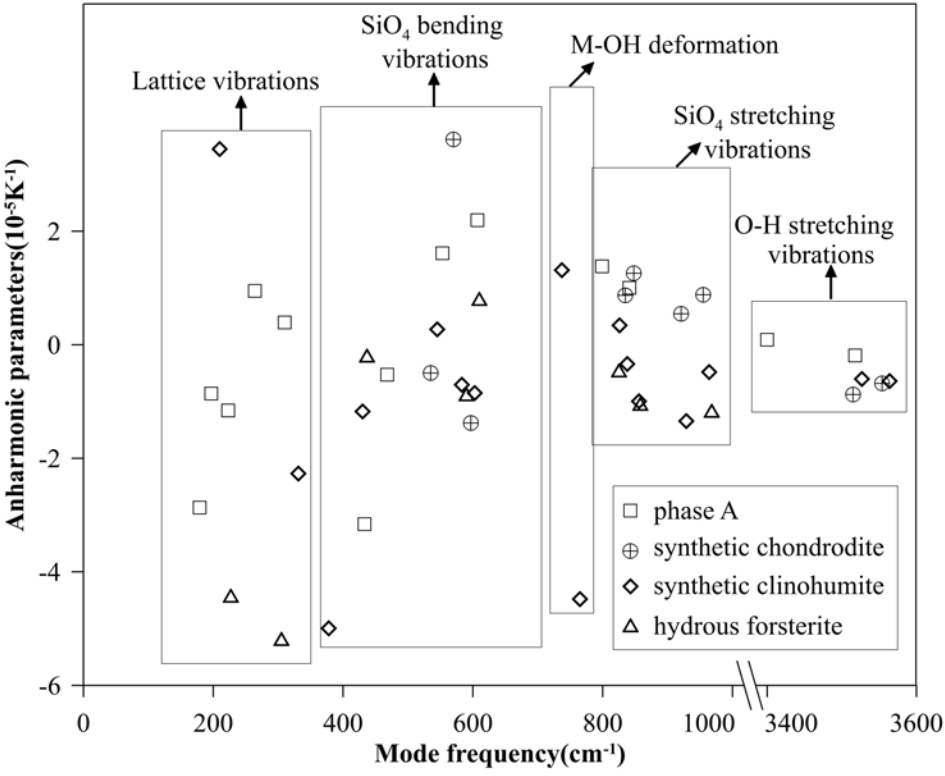
Lattice vibrations
SiO4 bending vibrations
M-OH deformation
SiO4 stretching vibrations
O-H stretching vibrations
phase A
synthetic chondrodite
synthetic clinohumite
hydrous forsterite
Anharmonic parameters(10-5K-1)
Mode frequency(cm-1)
2
0
-2
-4
-6
0
200
400
600
800
1000
3400
3600

Fig. 10

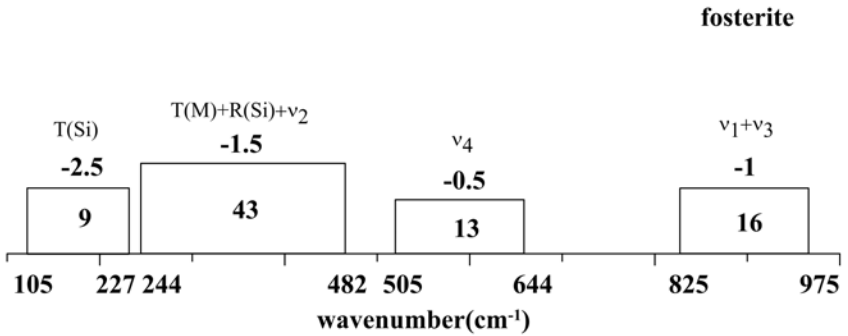
fosterite
T(Si)
-2.5
9
T(M)+R(Si)+ν2
-1.5
43
ν4
-0.5
13
ν1+ν3
-1
16
105
227
244
482
505
644
825
975
wavenumber(cm-1)

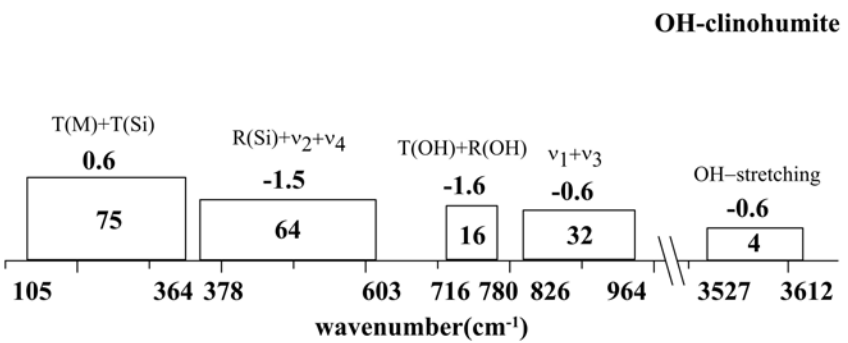
OH-clinohumite
T(M)+T(Si)
0.6
75
R(Si)+ν2+ν4
-1.5
64
T(OH)+R(OH)
-1.6
16
ν1+ν3
-0.6
32
OH−stretching
-0.6
4
105
364
378
603
716
780
826
964
3527
3612
wavenumber(cm-1)

(a)

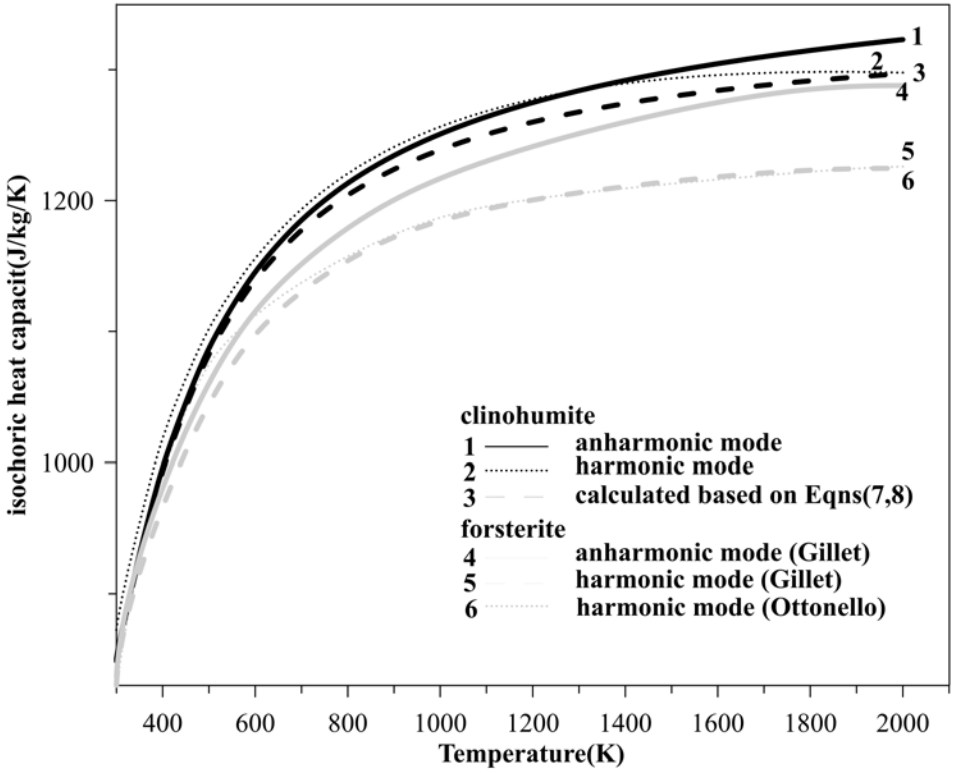
isochoric heat capacit(J/kg/K)
1200
1000
400
600
800
1000
1200
1400
1600
1800
2000
Temperature(K)
1
2
3
4
5
6
clinohumite
1 anharmonic mode
2 harmonic mode
3 calculated based on Eqns(7,8)
forsterite
4 anharmonic mode (Gillet)
5 harmonic mode (Gillet)
6 harmonic mode (Ottonello)

(b)

Fig. 11